UNIVERSITY OF CALIFORNIA
RIVERSIDE

Approaches to Improving the Capacity, Rate Capability, and Longevity of Next Generation Lithium-ion Batteries

A Dissertation submitted in partial satisfaction
of the requirements for the degree of

Doctor of Philosophy

in

Materials Science and Engineering

by

Jeffrey Michael Bell

June 2018

Dissertation Committee:

Dr. Cengiz Ozkan, Co-Chairperson
Dr. Mihri Ozkan, Co-Chairperson
Dr. Sandeep Kumar
Dr. Nanpeng Yu

The Dissertation of Jeffrey Michael Bell is approved:

_____

_____

_____

Committee Co-Chairperson

_____

Committee Co-Chairperson

University of California, Riverside

Acknowledgements

The text of this dissertation, in part or in full, is a reprint of the material as it appears in "Free-Standing Ni-NiO nanofiber cloth anode for high capacity and high rate Li-ion batteries" Nano energy 2015, "Advanced Sulfur-Silicon Full Cell Architecture for Lithium-Ion Batteries" Nature Scientific Reports 2017, and "Plateau Targeted Conditioning: An Additive-Free Approach Towards Robust SEI Formation in Li-S Batteries for Enhanced Capacity and Cycle life" Nano Energy 2018. The co-author Cengiz Ozkan and Mihri Ozkan listed in that publication directed and supervised the research which forms the basis for this dissertation.

Free-Standing Ni-NiO nanofiber cloth anode for high capacity and high rate Li-ion batteries:

-Authors thank Mathias Rommelfanger for his help with TEM analysis.

Advanced Sulfur-Silicon Full Cell Architecture for Lithium-Ion Batteries:

-We gratefully acknowledge financial support from the University of California, Riverside, CA, and Vantage Advanced Technologies LLC, Corona, CA. We also would like to thank Leon Peng and Andrew Scott for technical assistance.

Plateau Targeted Conditioning: An Additive-Free Approach Towards Robust SEI Formation in Li-S Batteries for Enhanced Capacity and Cycle life

-We gratefully acknowledge financial support from the University of California, Riverside, CA, and Vantage Advanced Technologies LLC, Corona, CA.

ABSTRACT OF THE DISSERTATION

Approaches to Improving the Capacity, Rate Capability, and Longevity
of Next Generation Lithium-ion Batteries

by

Jeffrey Michael Bell

Doctor of Philosophy, Graduate Program in Materials Science and Engineering
University of California, Riverside, June 2018
Dr. Cengiz Ozkan, Co-Chairperson
Dr. Mihri Ozkan, Co-Chairperson

Electrochemical storage has gained momentum amid increasing concerns for a cleaner, more environmentally friendly future. Currently, lithium ion battery systems do not meet the requirements to quell the increasing concerns and it is therefore imperative to move in a new direction. Top contenders for 'beyond lithium' is lithium-sulfur (Li-S) and silicon (Si) and other various metal oxides. In order for these materials to be adopted, it is necessary to use alternative methods of synthesis, varying architectures, and different approaches to formation. Herein, different methods for improving sulfur, silicon, and nickel oxide capacity, rate capability, and longevity will be explored using electrochemical and physical characterization.

Table of Contents

List of Figures

List of Tables

1. Introduction

Research that is focused on improving the energy density of lithium-ion batteries using new materials is increasing in correlation to the expectations and desires of society for a greener future. As it currently stands, current lithium-ion battery technology performance metrics aren't capable of keeping pace with improvements in renewable energy and consumer electronics. The requirements for renewable energy (solar, wind, hydro) can be broken down into frequency balancing and load balancing, where frequency balancing requires high rate capabilities and load balancing requires high capacities. Consumer electronic seek high capacities, quicker recharge times, and improved safety. In order to keep pace across the renewable energy sector and consumer electronics (such as EVs), lithium-ion batteries need to improve dramatically in safety, capacity, rate capability and longevity by either improving the materials, structure, or architecture.

The next generation of battery materials can be divided between cathode, anode, and electrolyte. For Cathode materials of interest, lithium sulfide (Li_2S) and sulfur (S) are especially interesting with theoretical capacities of 1166 mAh/g and 1675 mAh/g respectively. This is a stark contrast to the capacity of current generation cathodes, such as Lithium Nickel Manganese Aluminum Oxide (NMC) at 170 mAh/g. Although lithium sulfide and sulfur's capacity is six time that of current generation cathodes, the material systems themselves suffer from a broad range of limitations preventing possible

commercialization. These include polysulfide shuttling, poor conductivity, and volumetric expansion. Polysulfide shuttling is a result of long chain polysulfides (Li_2S_8-Li_2S_4) having a high solubility in the ether based electrolyte. As a result, the long chain polysulfides dissolve in the electrolyte causing degradation of the cathode and systemic capacity loss. The poor conductivity stems from the material properties of lithium sulfide and sulfur. Volumetric expansion is a result form S_8 lithiation to Li_2S, the resulting density changes corresponds to a volume change of up to 83%. Volumetric expansions of lithium sulfide and sulfur results in mechanical pummeling, degrading the cathode over its lifetime. Current approaches to alleviating issues in lithium sulfide and sulfur are to add a highly porous and conductive carbon structures to alleviated conductivity and expansion issues coupled with thin layers of 2D materials to prevent polysulfide shuttling.

Anode materials of interest for next generation lithium ion batteries include silicon and pure lithium metal. Silicon (Si), a metalloid, has a theoretical capacity of 4200 mAh/g with a stoichmetric ratio of $Li_{3.75}Si$ while pure Lithium's theoretical capacity is 3879 mAh/g. Similar to next generation cathodes of interest, silicon and lithium suffer from several drawbacks. Silicon suffers from extreme volumetric upwards of 400% coupled with low conductivity. In order to combat volumetric expansion and low conductivity, researchers have been exploring the use carbon coatings in addition to using a elastomers in the slurry. Although these have been successful to a certain extent, further research is needed in order to achieve a cycle life greater than 100 cycles.

Lithium faces similar challenges to silicon, but to a greater extent. While lithium may be regarded as the “Holy Grail” of anodes, researchers must overcome infinite volumetric expansion and dendrite formation of the lithium metal anode. For lithium metal, volumetric expansion is directly related to dendrite formation. Dendrite formation results from pitting and plating occurring on the lithium metal. As the cell is cycled, the pits deepen while the plates continue to grow, eventually forming root like structures over the anode that will pierce the separator, thus shorting the cell. As a result of the pitting and plating, the morphology of the lithium metal anode changes with every cycle thus creating infinite volumetric expansion. Although changing the cathode and anode will be a big step towards increasing the capacity, longevity, rate capability, and safety of lithium-ion batteries, the electrolyte plays a crucial role in ensuring these parameters are met.

Electrodes can be divided into two different form factors, solids and liquids. Solid electrolytes can be further divided into Pervoskite, Granite, lithium super ionic conductor (LISICON), and sodium super ionic conductor (NASICON). Liquid electrolytes are broken down into categories based on their salt, solvent, and additives can break down liquid electrolytes. In the case of a lithium sulfide and sulfur, liquid electrolytes can be broken down further into high solvating and low solvating. Depending on the electrolyte chosen, ionic conductivity and material degradation can be severely affected, but as this is not the focus of this thesis it will not be covered.

Herein, methodologies for synthesizing, improving, and altering of various material systems will be explored for nickel oxide (NiO), silicon, and sulfur. In addition, work exploring the combination of sulfur and silicon systems will be addressed by looking into alternative methods for cell configuration. Finally, an uncommonly explored area of cell formation for Li-S will be presented laying out findings that indicate strong room for growth and improvement in terms of cell performance and stability.

2. Transition Metal Oxide batteries

2.1 Free-standing Ni-NiO Nanofiber Cloth Anode for High Capacity, High Rate Li-ion Batteries

(See Next Page)

Free-standing Ni-NiO Nanofiber Cloth Anode for High Capacity, High Rate Li-ion Batteries

Jeffrey Bell[1], Rachel Ye[2], Kazi Ahmed[3], Chueh Liu[1], Mihri Ozkan[3], and Cengiz Ozkan[2]

[1]Material Science and Engineering Program, University of California Riverside, 900 University Ave. Riverside, CA 92521

[2]Mechanical Engineering Department, University of California Riverside, 900 University Ave. Riverside, CA 92521

[3]Electrical and Computer Engineering Department, University of California Riverside, 900 University Ave. Riverside, CA 92521

Abstract

Here we present a low cost, free-standing, high capacity, stable, and environmentally benign nickel-nickel oxide (Ni-NiO) nanofiber cloth anode for Li-ion batteries. Ni-NiO nanofibers are fabricated by simple electrospinning and thermal oxidation processes which create a free-standing, core-shell nanofiber structure. The nickel backbone mitigates poor conductivity issues observed in Li-ion anodes due to repeated volume change during lithiation/delithiation. The Ni-NiO nanofiber anode possesses a high surface area compared to that of a slurry cast electrode which helps facilitate Li-ion

diffusion into the active material. Electrochemical impedance spectroscopy indicates improved capability of current collecting metal (nickel in this case) to withstand volume change in our free-standing structure. Furthermore, scanning electron microscopy indicates the stability of the Ni-NiO nanofiber cloth anode in excess of 400 charge/discharge cycles, partly evidenced by the stable evolution of solid-electrolyte interphase. As an anode, the Ni-NiO nanofiber cloth shows impressive results with a gravimetric capacity of 1054 mAh g^{-1} at a current density of 2154 mA g^{-1} or 3C (1C=718 mA g^{-1}), a long cycle life of more than 1500 cycles, and exceptional stability throughout its cycle life with a Coulombic efficiency >99%. Performance evaluation enables the Ni-NiO cloth material for next-generation high capacity, high rate, stable, and environmentally benign Li-ion batteries.

1.1 Introduction

Stable high rate, high capacity, and environmentally safe Li-ion battery (LIB) electrodes are at the center of research interest in energy storage.[1-3] LIBs outperform other competing battery technologies currently in the market for portable electronics and are becoming the technology of choice to power next generation electric vehicles.[2,4-7] Research seeks to meet market demands for cost effective, safe, and high performing LIBs through investigating novel materials possessing various nanostructures.[8-10] LIB electrodes often consist of conductive additives, binder, current collector, and active material.[7,11-13] One method of increasing the overall gravimetric capacity of a LIB cell is

to eliminate the use of conductive additives and binders in the system. Binders and conductive additives can be replaced by utilizing free-standing electrodes with an embedded current collector. A free-standing electrode incorporates the current collector into the electrode architecture.[14] This reduces the need for the use of binders or conductive additives. However, many of the active materials used are neither conductive enough nor capable of adhering themselves onto the current collector.[4-6] Some free-standing electrodes based on carbon-textile or carbon-based paper**,** carbon-based nano-scaffolds, and electrospun fibers have been shown.[15-18] These exhibit high capacities, fast cycling rates and long cycle lives but suffer from lengthy thermal oxidative stabilization, carbonization, and mechanical fragility.

Candidates for replacement of graphite as an anode - with a theoretical capacity of 372 mAh g^{-1} include silicon, tin-based materials, a variety of transition metal oxides, and Li metal.[5-7] These materials exhibit larger capacities than graphite but suffer from potential drawbacks that span from volumetric expansion to poor Coulombic efficiency. Silicon, tin-based materials, and transition metal oxides suffer from volume changes during lithiation/delithiation or from poor conductivity.[7,19] The volume change during cycling causes degradation in the electrode's morphology over the course of its cycle life.[20] As a result, the active material loses contact with the conductive network and the SEI layer degrades. Degradation of the SEI layer results in continual, thicker re-formation of the SEI layer that consumes electrolyte and lithium.[21] Loss of contact with

the conductive network and degradation of the SEI layer leads to a decrease in capacity and Coulombic efficiency. Li metal is the ideal material for an anode based on its high capacity, high conductivity, and its lack of need for diffusion/intercalation. The challenges facing Li metal as an anode include repeated formation of Li dendrites during lithiation/delitiation, low Coulombic efficiency, and safety concerns.[21] Metal oxides show promise in alleviating many of the problems faced by next generation Li-ion batteries, but not without the correct electrode design.

Nickel (II) oxide (NiO) is emerging as a promising anode material for high capacity, long cycle life, low cost, and environmentally benign Li-ion batteries.[7] This material system exhibits a high theoretical capacity of 718 mAh g^{-1} and an ability to be easily transformed into various 3D structures for use in innovative electrodes.[12] However, the electrochemical performance of NiO is limited by large variations in volume during lithiation/delithiation and poor conductivity. To combat this issue, various nanostructures have been employed to improve the electrochemical performance such as nanofibers, core-shell nanowires, and carbon structures coated in nickel oxides.[12,22,23] Many of these structures exhibit a long cycle life up to thousands of cycles, exceptional cycling rates up to 10C or high capacities up to 800 mAh g^{-1}.[12,24,25] Although these structures have their advantages, none of them combine an outstanding cycle life, high charge current density, and exceptional capacity with a free-standing electrode.

Here we present a novel free-standing Ni-NiO nanofiber cloth anode synthesized by electrospinning and processed by simple heat treatments that address the aforementioned problems. The free-standing Ni-NiO nanofiber cloth anode exhibits a long cycle life of more than 1500 cycles, a high capacity of 1054 mAh g^{-1} at a relatively fast cycling rate of 3C (1C=718 mA g^{-1}), and a Coulombic efficiency >99%. Most impressively though, the Ni-NiO fiber cloth anode maintained a high capacity of 1108 mAh g^{-1} for more than 1500 cycles at 3C with minimal changes in the morphology post cycling. To the best of our knowledge, an electrospun free-standing Ni-NiO nanofiber cloth anode with a nanostructured metal embedded within the active material serving as the current collector with such outstanding performance has not been previously reported.

1.2 Experimental Details

1.2.1 Material Synthesis

For the preparation of the Ni-NiO fibers, 132 mg mL^{-1} of $Ni(OCOCH_3)_2 \cdot 4H_2O$ and 66 mg mL^{-1} of polyvinylpyrrolidone (PVP, 1 300 000 g mol^{-1}) were mixed in ethanol for 30 minutes at 70^0C. After the solution was mixed thoroughly, the solution was transferred into a 5 mL syringe and electrospun using the Inovenso Ne300 Nanospinner. The feeding rate of the solution was 0.6 ml hr^{-1} and the spinning potential was 6 kV, while the needle collector distance was 11cm. After the fiber was spun, it was calcined within an Alumina tube at 400^0C for 6 hours in air at a heating rate of 0.66^0C min^{-1} with 2 hours of thermal oxidation stabilization at 200^0C to obtain pure nickel oxide fibers. Thermal

oxidation in total took 16h to complete. The nickel oxide fibers were then reduced to nickel fibers by hydrogen reduction at 20 Torr and 400^0C for 90 minutes with a heating rate of 13^0C min^{-1} under a constant flow of Ar/H_2 (1:2 volume ratio). The nickel fibers were cooled down at a cool rate of 20^0C min^{-1}. Lastly, the nickel fibers were re-calcined at 350^0C in air for 30 min with a heating rate of 20^0C min^{-1} to get the Ni core, NiO shell fibers.

1.2.2 Physical Properties Characterization

The morphology of the woven fibers was observed by scanning electron microscopy (Philips XL-30) and transmission electron microscopy (FEI Tecanai12). The synthesized fibers elemental makeup was characterized by X-ray powder diffraction (PANanalytical Empyrean) using Cu-K radiation and EDS (Electron Diffraction Spectroscopy). The makeup of the structure was determined by energy dispersive spectroscopy (Nova NanoSEM 50 Series).

1.2.3 Electrochemical Characterization

Electrochemical measurements were carried out using a type 2032 coin cell with lithium foil acting as the counter electrode and a Celgard 25um 3501 PP separator. The working electrode was prepared by cutting out pieces of Ni-NiO cloth. The resulting cloth was then placed inside the type 2032 coin cell. Assembly of the cells took place in an Argon filled glove box (H_2O < 0.5 ppm, O_2 < 0.2 ppm, VAC). The electrolyte consisted of 1m

$LiPF_6$ dissolved in a mixture of Ethylene Carbonate (EC) and dimethyl carbonate (DMC) (1:1 wt) containing 1% wt additive of vinyl carbonate (VC). The loading of the cells was 0.4-0.6 mg cm^{-2}. The type 2032 coin cells were Galvanostatically discharged and charged using an Arbin potentiostat with a voltage range of 0.01-3.0 V vs. Li/Li^+. CV tests were carried out between 0.01-3.0V using a sweep rate of 0.5 mV s^{-1} on an Bio-Logic VMP3. EIS(Bio-Logic VMP3) was carried out at a frequency range that varied from 10 mHz to 100 kHz with an AC signal amplitude of 10 mV. Galvanic cycling, CV, and EIS measurements were all carried out at room temperature (23^0C).

1.3 Results and Discussion

The Ni-NiO fibers were synthesized by electrospinning a sol-gel solution consisting of Nickel acetate ($Ni(CH_3CO_2)_2$) and polyvinylpyrrolidone (PVP) dissolved in ethanol. Oxygen was introduced into the nanofiber structure though calcination at 400^0C in air. The introduction of oxygen results in the formation of nickel oxide (NiO) nanofibers.[22,26-29] The NiO fibers were reduced at 400^0C by hydrogen flow at 20 torr resulting in a dull grey nickel nanofiber cloth. A NiO shell was formed through partial calcination at 350^0C in air for half an hour.[30] A detailed schematic of the process is illustrated in Figure 1 along with images of the processed materials. Low temperature thermal treatments were utilized in order to keep the grain sizes small. Small grains act as a contributor to facilitate the formation of an advantageous polymer/gel-like coating that forms during cycling.[31,32]

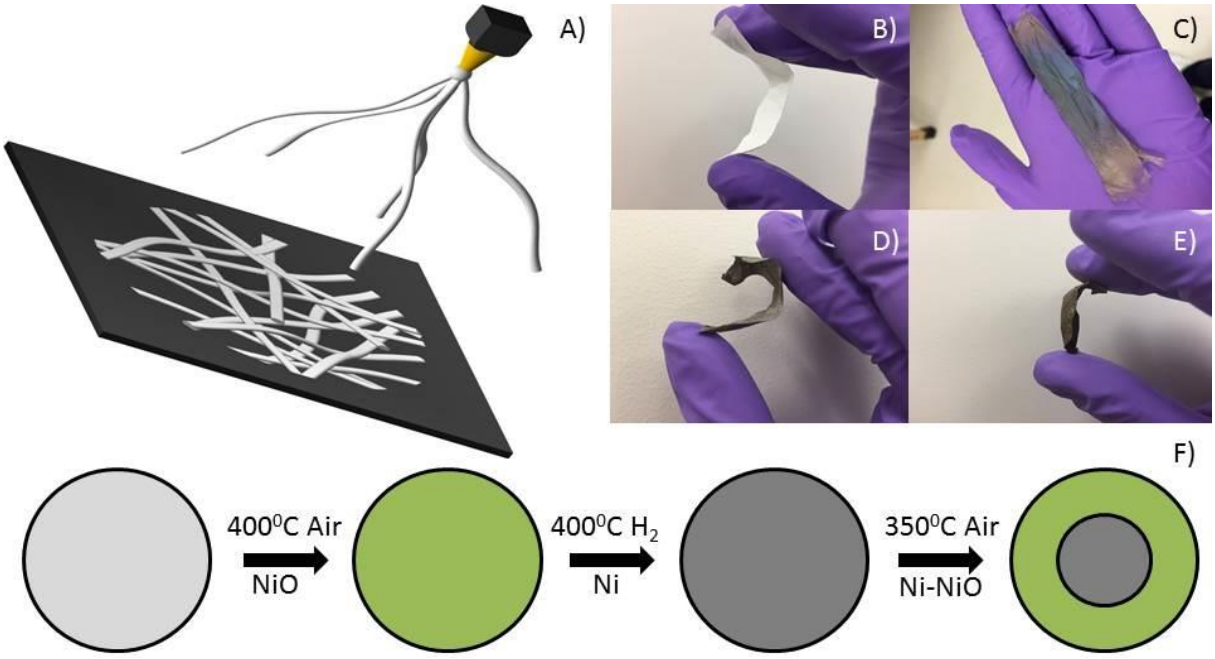

Figure 1. A) Electrospinning process. B) As spun nanofiber matte. C) Calcined NiO nanofibers. D) Reduced Ni nanofibers. E) Partially calcined Ni-NiO nanofibers. F) Schematic of the thermal oxidation/reduction process.

Changes in the morphology resulting from thermal treatment were studied using SEM shown in Figure 2. The as spun nanofibers in Figure 2A show smooth nanofibers with a diameter of approximately 400 nm. Shown in Figure 2B, the nanofiber diameter is approximately reduced in half to 200 nm post calcination. This results from the loss of acetate groups and polymer during thermal treatment. Post hydrogen reduction, the smooth morphology was lost as a result of a volume change from NiO to Ni, shown in Figure 2C.[24,25,30] Figure 2D shows the formation of a NiO layer on the surface of the Ni nanofibers after partial calcination.

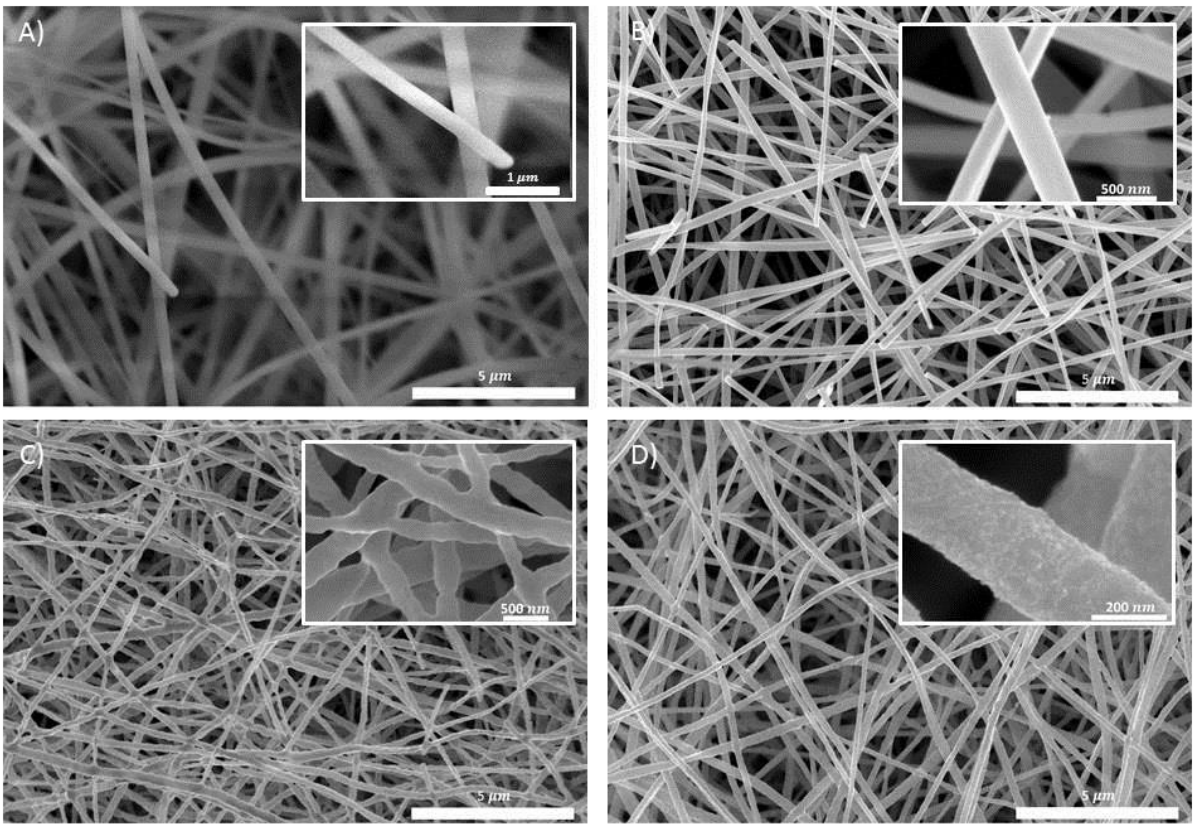

Figure 2. A) SEM image of pre calcined fibers. B) SEM image of NiO fibers post calcination. C) SEM image of Ni fibers post hydrogen reduction. D) SEM image of Ni-NiO fibers with inset image of fibers surface.

The representative Transmission Electron Microscopy (TEM) images shown in Figure 4 reveals a distinct oxide layer attributed to nickel oxide on the Ni-NiO fibers, roughly 20 nm in thickness. SAED confirms the presence of an amorphous oxide layer and a crystalline nickel core. The uneven surface morphology of the nickel core results from the reduction of NiO to Ni. The reduction creates nickel nanocrystals that are tightly

bound together, which acts as the backbone of the Ni-NiO cloth fibers. The crystalline nickel and amorphous oxide layer TEM results shown in Figure 3 is in agreement with the XRD and EDS results shown in Figure 4.

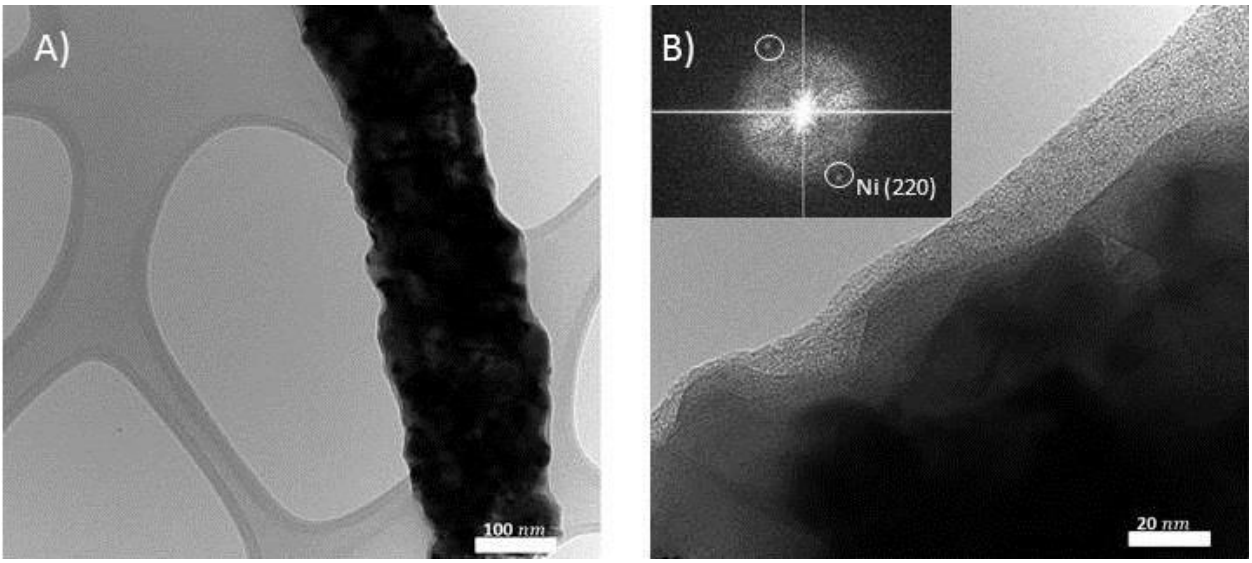

Figure 3: A) TEM image of Ni-NiO cloth fiber. B) TEM image of Ni-NiO cloth fiber showing NiO thickness with inset SAED.

The chemical composition of the Ni-NiO nanofibers were confirmed by XRD and EDS. Figure 4A shows the XRD pattern of the fibers at different processing phases. The three XRD patterns correspond to NiO, Ni, and Ni-NiO nanofibers post calcination, reduction, and partial-calcination respectively. In Figure 4A, the peaks at 37.1°, 43.1° and 62.6° represents the (111), (200), (220) planes of the NiO face-centered cubic crystal structure. The peaks at 44.5°, 51.8° and 76.4°coincides with the XRD pattern for nickel.[33] These peaks correspond to the (111), (200) and (220) planes of the face-

centered cubic Ni crystals respectively. The XRD pattern for Ni-NiO nanofibers shows all the peaks from the previous two XRD patterns. The peaks at 37.1°, 43.1° and 62.6° for NiO are weaker because of the amorphouse characteristic, while the peaks at 44.5°, 51.8° and 76.4° are stronger for Ni because of its high crystallinity. No carbon peaks were detected during XRD analysis of the Ni-NiO cloth nano fibers. This shows that the Ni-NiO fibers are only composed of Ni and NiO crystals and all excess carbon was burnt off.[22,34] The XRD results are confirmed by both EDS and TEM shown in Figure 4B, Figure 3. The EDS spectra in Figure 4B shows the sole presence of nickel and oxygen within the structure. EDS mapping shows the nickel and oxygen distribution throughout the structure. The distribution of oxygen throughout the structure is represented by the inset image in Figure 4C, giving a total of 2.28 wt% oxygen distributed evenly across the surface of the Ni-NiO nanofibers.

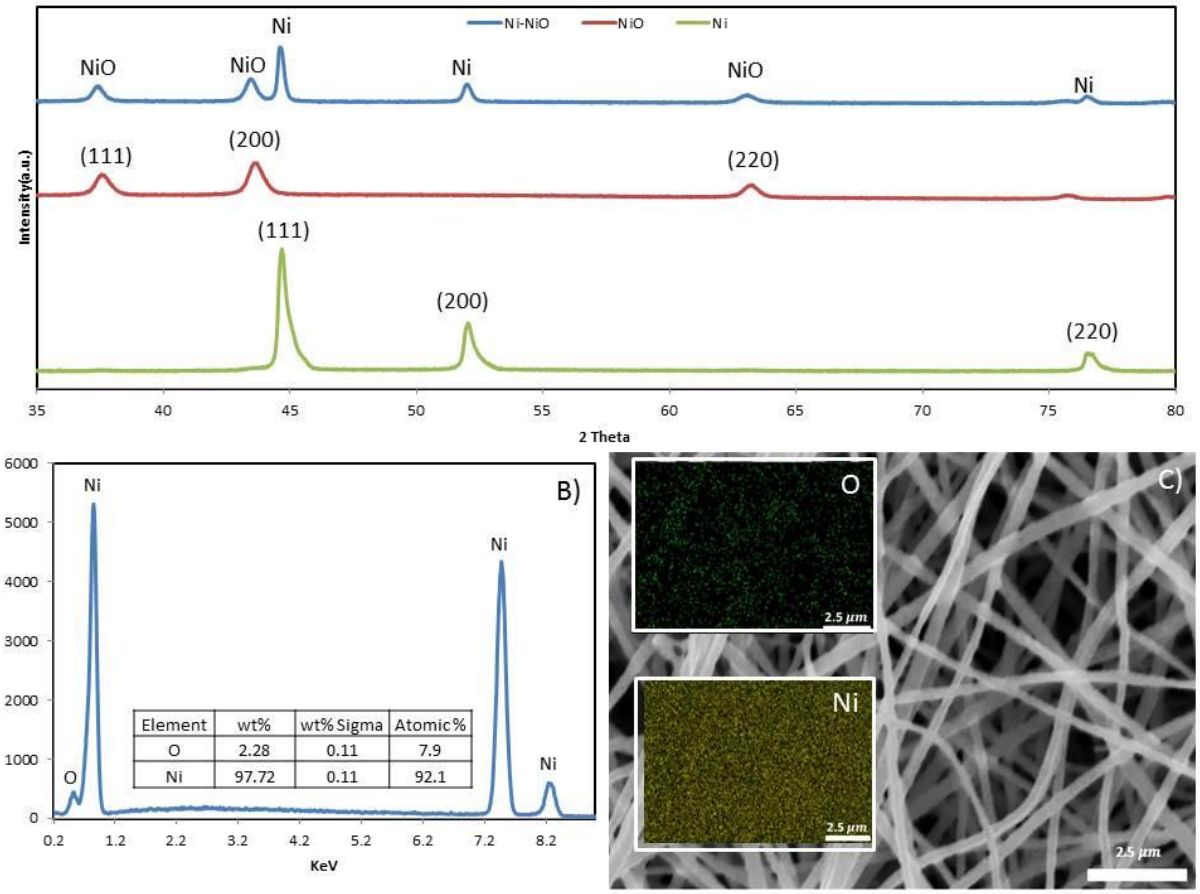

Figure 4. A) X-ray powder diffraction of NiO Fibers, Ni Fibers, and Ni-NiO fibers. B) EDS spectra of Ni-NiO fibers with inset display showing weight percentages after partial calcination. C) SEM image of EDS mapped area with inset images of elemental mapping.

The electrochemical properties of the Ni-NiO nanofiber anode was evaluated using galvanostatic cycling, cyclic voltammetry (CV) and electrochemical impedance spectroscopy (EIS). The weight of NiO was calculated by the mass-change measurement, assuming the change mass from pure Ni fibers to partially calcined Ni-

NiO fibers are purely due to the introduction of oxygen. The calculated weight was used to determine capacity and C rate. The CV was performed at a scan rate of 0.5 mV s^{-1} over cycles 1-10 and cycles 161-170. Figure 5A and Figure 5B show the CV profiles for cycles 1-10, 161-170 respectively. As shown in Figure 5A, the CV profile for cycles 2-10 exhibit similar peaks indicating stable cycling performance over the first few cycles.[24] The large difference in the CV profiles for cycles 1 and 2 is most notably the large peak at 0.5 V. The large cathodic peak around 0.5 V is attributed to the formation of the solid electrolyte interface (SEI) layer, the reduction of nickel oxide to nickel, and the formation of amorphous Li_2O ($NiO + 2Li^+ + 2e^- \rightarrow Ni + Li_2O$).[12,24] The cathodic peak at 0.5V is followed by an anodic peak at 2.25V. The anodic peak represents the decomposition of the polymer/gel-like layer and the reversible reduction of Ni^0 to Ni^{2+}. For the remainder of the cycles after the first, the anodic peak shifts to 1 V. The CV profiles for cycles 161-170 is very similar to cycles 2-10 although a current difference exists. The difference in current is attributed to a change in the peak current which alludes to a higher capacity and reactivity.[35] This coincides with the increase in capacity seen after 160 cycles shown in Figure 6. The similarities in the curves indicate a very stable cycling performance and the stable formation of the SEI layer after 10 cycles. The stable cycling performance is attributed to the nickel backbone's ability to prevent damage caused by mechanical stress and strain from volume expansion/contraction of 95.68% during lithiation/delithiation of NiO.[36] As a result, the pulverization resistant structure provides a stable conductive network for NiO that is not prone to degradation

during lithiation/delithation.[37] This is proven by a constant equivalent series resistance (ESR) of 2.7 for all cycles resulting in an impressive cyclability.

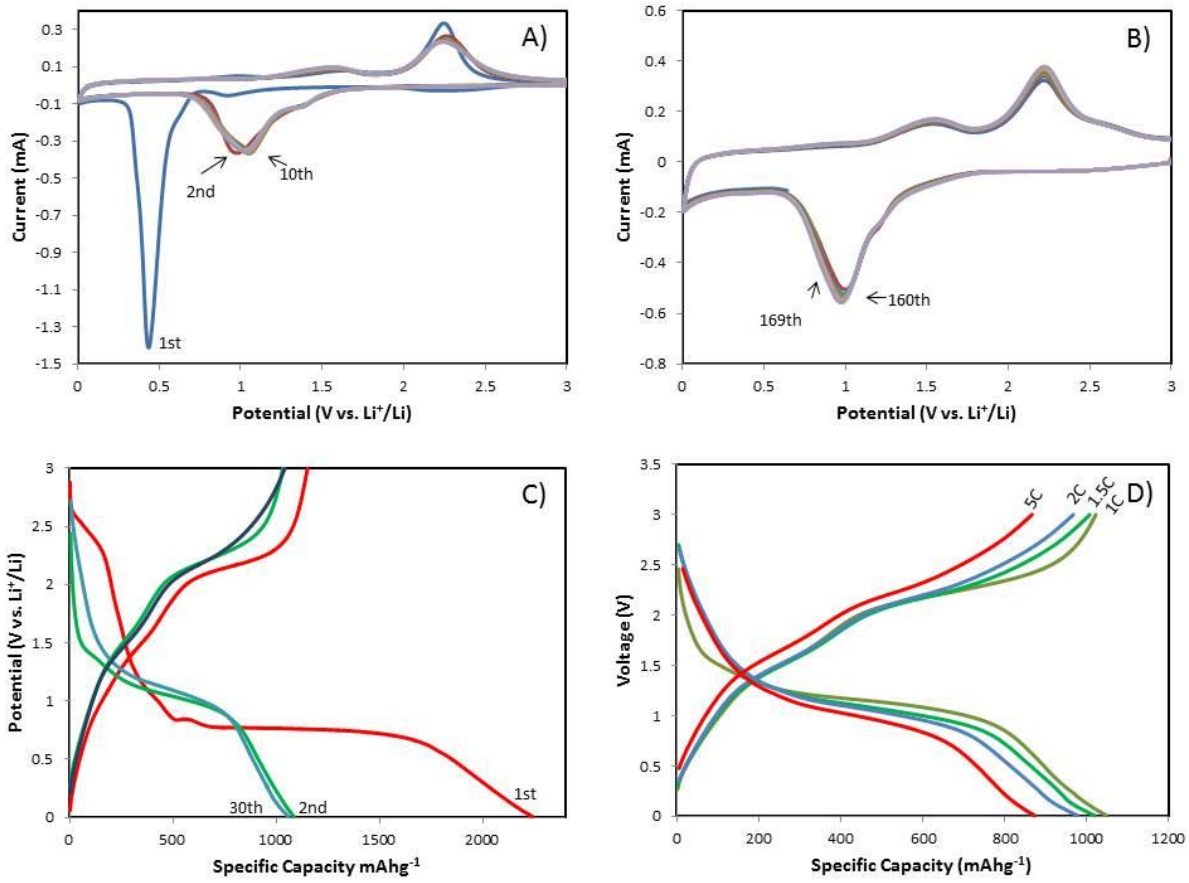

Figure 5. A) CV of cycles 1-10 at a scan rate of 0.5 mVs^{-1}. B) CV of cycles 160-169 at a scan rate of 0.5 mVs^{-1}. C) Galvonastic voltage profiles for Ni-NiO fibers at 1C for selected cycles. D) Galvonastic voltage profiles for Ni-NiO fibers at selected C-rates.

The charge-discharge profiles for the Ni-NiO nanofiber electrode between 0.01-3.0V is shown in Figure 5. Figure 5C shows the charge-discharge profiles at a rate of 1C. The

potential of the electrode during its first discharge in Figure 5C exhibits a long plateau at 0.85V. The long plateau is attributed to the formation of the SEI layer, initial reduction of NiO to Ni, and the formation of amorphous Li_2O.[12] According to the voltage profile of Figure 5C, the polymer/gel like layer starts to form during first discharge cycle around 0.85V, which is usually 0.7V for NiO, and 1.3V for all other cycles. This is consistent with the CV profiles of NiO reported in literature.[25,30,32,37] The increased voltage plateau from 0.7V to 0.85V for the first cycle results from the eased reaction of NiO with Li^+ to form Ni and Li_2O.[31,32] The main cause of the eased reaction of NiO with Li^+ is the small grain sizes which promote the growth of a polymer/gel-like layer. The polymer/gel-like layer is formed when lithium ions form lithium alkyl carbonate with the electrolyte instead of reacting with the NiO, the lithium alkyl carbonates then build up on the surface of the electrode, forming a polymer/gel like layer.[31] The advantages in the formation of these polymer/gel-like layers are the promotion of a higher capacity and better stability. Firstly, the polymer/gel-like layer causes pseudocapacitance behavior.[31] Psuedocapacitance reactions are known to be highly reversible and to be a source of extra capacity.[31] Secondly, the polymer/gel-like layer holds the active material tightly to the nickel backbone, not only improving the structures conductivity, but also holding the materials tightly together to help maintain its original morphology.[31] As shown in Figure 7, the Ni-NiO nanofiber electrode retains its original morphology after 400 cycles at 3C, allowing the electrode to retain a greater portion of its capacity. This polymer/gel like layer remains attached to the surface of the electrode during the remainder of the

discharge. During the charge cycle the polymer/gel like layer dissolves when the voltage exceeds 2V contributing to the change in the charge plateau from 2 V to 2.3 V.

The charge-discharge profile for cycles 2 and 30 in Figure 5C exhibits similar curves alluding to the stability of the electrode under a cycling rate of 1C. Increasing the cycling rates for the Ni-NiO nanofiber battery results in a higher charge plateau and lower discharge plateau shown in Figure 5D. The change in plateaus is a result of a current density increase, causing a rise in the overpotential of the battery.[24] Despite this, the charge-discharge curves for different cycling rates exhibit similar curves, a plateau between 1.4-0.7V shown in Figure 5D. The similarity in the plateaus correlates to the Ni-NiO nanofiber battery's excellent rate performance which is attributed to the rigidity of the nickel as a conductive network during higher cycling rates and the stable formation of the SEI layer. A stable conductive network enhances electrochemical activity by improving electron transport.[38] A stable SEI layer prevents the continual re-formation of a thicker SEI layer which reduces the ionic conductivity and greatly affects the rate capability.[31,39]

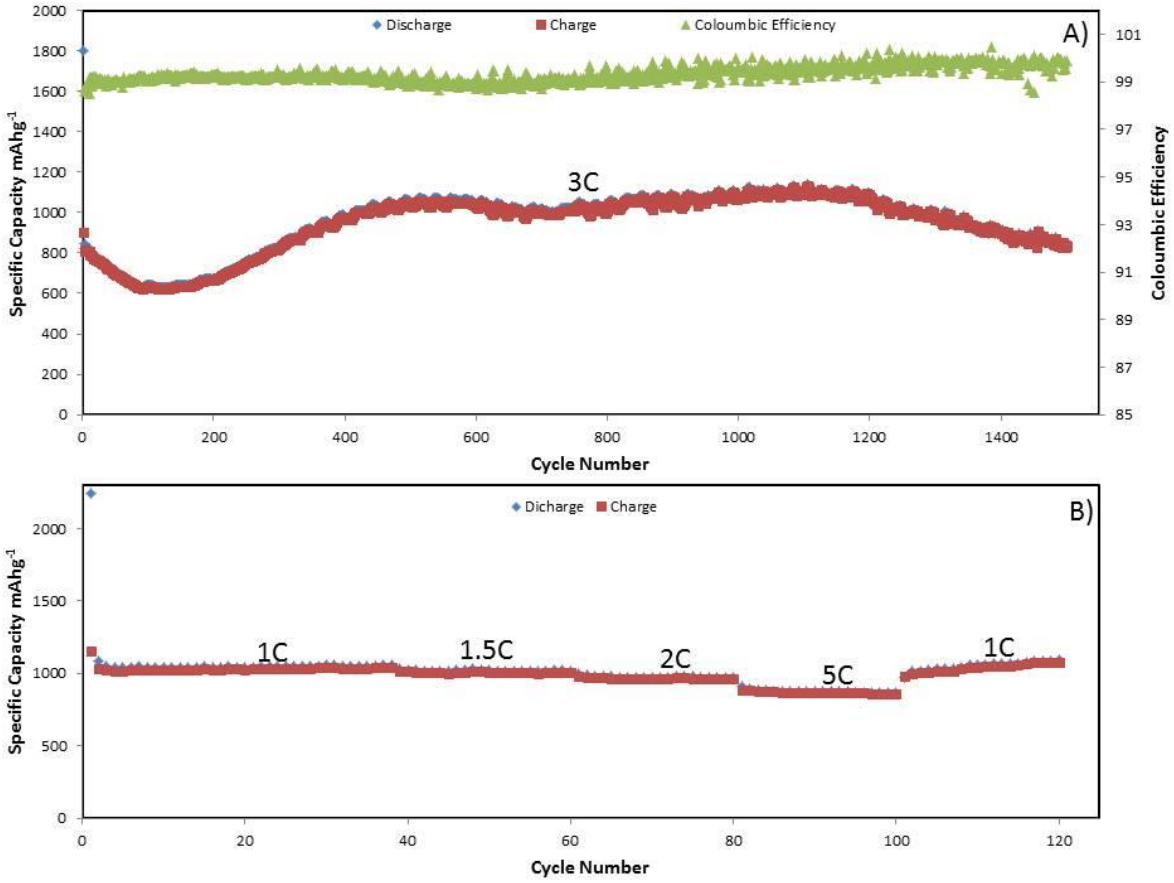

Figure 6. A) Deep Galvanostic cycling at 3C for more than 1000 cycles. B) Galvanostic cycling at 1C, 1.5C, 2C, and 5C over 120 cycles.

The Galvanostatic cycling was carried out in the potential window of 0.01 V – 3.0 V using a lithium metal wafer as the counter electrode. As in Figure 6A, the capacity was measured at a charging rate of 3C for all cycles. The Ni-NiO batteries show excellent stability and a Coulombic efficiency of >99%. The initial capacity is recorded at 1801 mAh g^{-1}, over the next 160 cycles the capacity decreases to 626 mAh g^{-1} before

increasing again over the next 840 cycles. The decrease in capacity is attributed to the high charge transfer resistance for the first 160 cycles. After 160 cycles, the capacity starts to increase due to a lower charge transfer resistance. This alludes to more of the surface area of the NiO being activated during lithiation/delithiation. The wave like fluctuation in capacity for cycles 100-1000 results from temperature changes occurring inside the room where galvanostatic cycling took place. The increase in capacity over 718 mAh g^{-1} can be attributed to a few possible explanations. Do et al. proposed that the increase in capacity results from decreased grain sizes promoting the amount of surface area for nickel oxide to form on the nickel backbone while also promoting the formation of a polymer/gel-like layer.[31,32] Other groups proposed that reversible growth of polymeric/gel-like layers is attributed to the kinetic degradation of the electrolyte.[9,31,32] We attribute the increase in capacity to the nickel backbone acting as an effective catalyst for electrolyte decomposition promoting the continual growth of polymeric/gel-like layers. This results in the battery lasting 1500 cycles while retaining all of its original capacity.

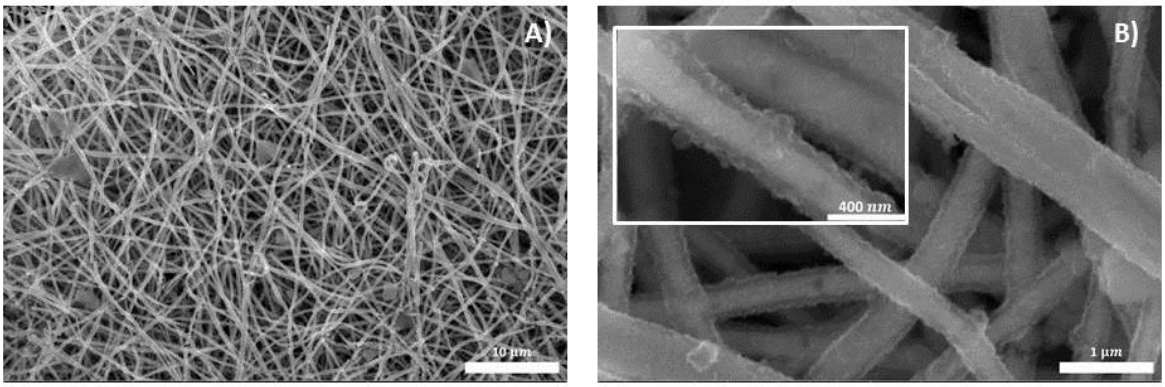

Figure 7. A) SEM image post 400 Cycles at 3C. B) SEM image post 400 Cycles at 3C with inset image magnifying fiber structure.

Rate capability is becoming an important factor in next generation LiBs. The rate capability of the Ni-NiO electrode was evaluated over various charge-discharge rates based on the amount of NiO for 120 cycles. Shown in Figure 6B, the first cycle exhibits a capacity of 2240 mAh g^{-1} and was charged-discharged at a rate of C/10 to ensure proper formation of the SEI layer. At a cycling rate of 718 mA g^{-1}, the Ni-NiO electrode exhibits a capacity of 1084 mAh g^{-1} that is well maintained for 60 cycles. Increasing the cycling rate to 1.5C, 2C, 5C for twenty cycles each results in a capacity loss of 2.5%, 6.5%, and 16.2% respectively when compared to the first 60 cycles. Full recovery of the original capacity is achieved when the cycling rate is returned to 1C. The Ni-NiO excellent rate capability is attributed to the stability of the electrode architecture under higher current densities, which maintains the conductivity of the system. Post cycling images in Figure

7 confirm the ability of Ni-NiO to maintain its initial morphology after 400 cycles at 3C, showing very little to no degradation. These results show that the free-standing Ni-NiO nanofiber, compared to that of a slurry cast electrode, has a longer life, a higher capacity, a better stability, and a better rate capability without damaging the electrode. This is due to the elimination of binders and conductive additives that would otherwise reduce the overall gravimetric capacity and the formation of a stable SEI layer that would otherwise reduce ionic conductivity.

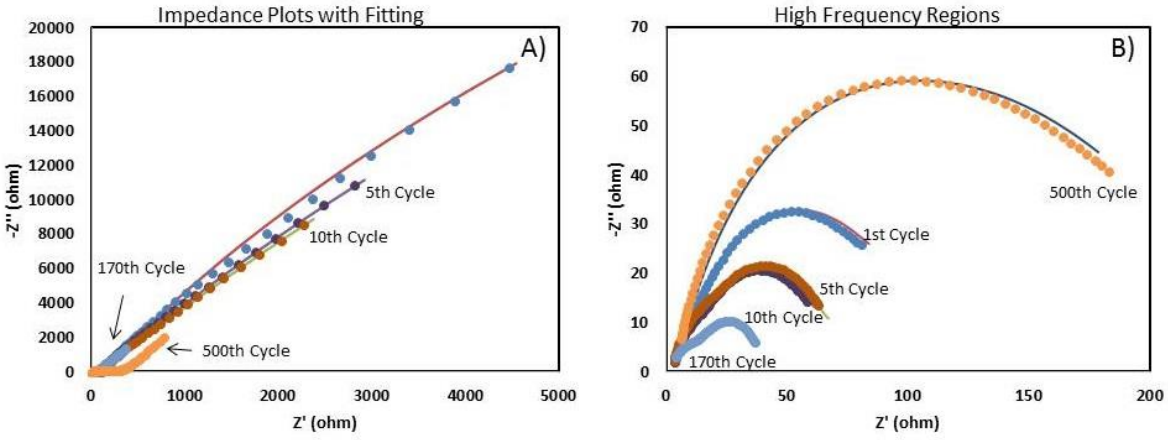

Figure 8. A) Shows complex impedance plots of Ni-NiO nanofiber anode for selected cycles. B) Shows high frequency regions of plots.

Complex impedance plots for the first ten cycles, near 170 cycles, and near 500 cycles were obtained by running potentiostatic electrochemical impedance spectroscopy

(PEIS). Electrochemical impedance spectroscopy (EIS) is a technique that applies a small sinusoidal of varying frequency and measures the resultant complex impedance. For the current investigation, 10 mV sinusoidal signals with frequencies ranging from 10 mHz to 100 kHz were applied. The plots contain the following distinct features: a high frequency intercept, two curves resembling semicircles at the higher frequency end, and a low frequency tail.[40] Figure 8A shows complex impedance plots for selected cycles and their model fits in accordance with the impedance of the electrical equivalent circuit shown in Figure 9. The high frequency intercepts represent electronic resistance in conductive material within the electrode in combination with the ionic resistance of the electrolyte, often presented as the equivalent series resistance (ESR). The Ni-NiO anode has a comparatively low ESR. More remarkably, this Ohmic resistance does not increase with cycling but stays at its initial value throughout 170 cycles, as shown in Table 1. This supports the claim that the nickel backbone provides a robust conductive network for the Ni-NiO anode that can withstand volume change during lithiation/delithiation without deterioration. Another thing to notice is the slight mismatch in fitting for the first cycle seen in Figure 8B. The equivalent circuit is composed of modeled parameters design to predict electrochemistry within a LIB cell. While the cell behavior becomes more predictable during later cycles, it may sometimes show evidence electrochemical steps that only are present during the first cycle (not represented in the equivalent circuit model).

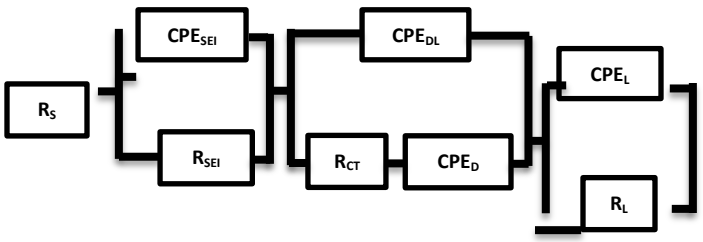

Figure 9. Electrical equivalent circuit used for fitting the complex impedance plots.

A low and stable value for ESR is indicative of excellent rate capabilities as observed during Galvanostic cycling. The first semicircle shape represents a frequency dependent complex impedance of the solid-electrolyte interphase that forms on the surface of the active material due to irreversible reactions involving lithium ions and solvent molecules. The diameter of the semicircle represents the resistance due to the solid-electrolyte interphase (SEI) layer, listed here as R_{SEI}.[41] The second semicircle contains impedance information on the electrochemical double layer that forms at the electrode-electrolyte interface.[42] The reaction kinetics that allows a battery to store energy takes place in this electrochemically active region. The diameter of this semicircle represents charge-transfer resistance or reaction resistance (R_{CT}) for the redox reactions involved in lithium ion exchange at the electrode.

Table 1. Lists relevant parameters obtained from EIS analysis of Ni-NiO anode.

Cycle	ESR	Rsei	Rct
1	2.7	5	88
2	2.7	7.5	65
3	2.7	7.5	62
4	2.7	8	60
5	2.7	9	53
10	2.7	10	56
170	2.7	10	27
501	3.5	60	150

Table 1 shows the evolution of R_{SEI} and R_{CT} with cycling for our Ni-NiO anode. The SEI resistance increases during the initial ten cycles while the electrochemically inert layer formed on active material surface. R_{SEI} stabilizes thereafter and maintains the same value through 170 cycles. Stable formation of the SEI layer is mandatory for good rate capabilities and cycling stability and is coherent in light of the excellent cycle life demonstrated in Figure 6B.[43] The sharp increase in SEI observed after 500 cycles may be due to the desolvation of gel/polymer layer formed on NiO surface, which led to new SEI formation. The R_{CT} decreases sharply during the initial cycles and continues to decrease through 170 cycles. The R_{CT} is expected to decrease with cycling in a high surface-area

electrode, as more of the active material surface is activated via repeated lithiation/delithiation of the electrode. The results of EIS confirm the crucial role of the nickel backbone in enhancing the stability of the free-standing Ni-NIO cloth anode and the stable formation of the SEI layer.

1.4 Conclusion

In summary, we have presented here a novel free standing Ni-NiO cloth anode synthesized by electrospinning followed by thermal oxidation/reduction processes. As an anode material for next generation LIBs, the free standing Ni-NiO cloth anode exhibits an outstanding high capacity of 1054 mAh g^{-1}, a long life of 1000 Cycles at 3C or 2154 mA g^{-1}, and an great rate capability up to 5C or 3590 mA g^{-1}. This work demonstrates a facile approach for achieving impressive performance using Ni-NiO cloth as an anode. The results presented here show that the free standing Ni-NiO cloth electrode is capable of replacing graphite anodes and providing the performance needed in LiBs for the next generation of portable electronics and electric vehicles.

References

1 Deng, D., Kim, M. G., Lee, J. Y. & Cho, J. Green energy storage materials: nanostructured TiO 2 and Sn-based anodes for lithium-ion batteries. *Energy & Environmental Science* **2**, 818-837 (2009).

2 Armand, M. & Tarascon, J.-M. Building better batteries. *Nature* **451**, 652-657 (2008).

3 Xu, G.-L., Li, J.-T., Huang, L., Lin, W. & Sun, S.-G. Synthesis of Co< sub> 3</sub> O< sub> 4</sub> nano-octahedra enclosed by {111} facets and their excellent lithium storage properties as anode material of lithium ion batteries. *Nano Energy* **2**, 394-402 (2013).

4 Etacheri, V., Marom, R., Elazari, R., Salitra, G. & Aurbach, D. Challenges in the development of advanced Li-ion batteries: a review. *Energy & Environmental Science* **4**, 3243-3262 (2011).

5 Choi, N. S. *et al.* Challenges Facing Lithium Batteries and Electrical Double-Layer Capacitors. *Angewandte Chemie International Edition* **51**, 9994-10024 (2012).

6 Goodenough, J. B. & Kim, Y. Challenges for rechargeable Li batteries†. *Chemistry of Materials* **22**, 587-603 (2009).

7 Reddy, M., Subba Rao, G. & Chowdari, B. Metal oxides and oxysalts as anode materials for Li ion batteries. *Chemical reviews* **113**, 5364-5457 (2013).

8 Xu, J., Dou, S., Liu, H. & Dai, L. Cathode materials for next generation lithium ion batteries. *Nano Energy* **2**, 439-442 (2013).

9 Zhang, W.-J. A review of the electrochemical performance of alloy anodes for lithium-ion batteries. *Journal of Power Sources* **196**, 13-24 (2011).

10 Mukherjee, R., Krishnan, R., Lu, T.-M. & Koratkar, N. Nanostructured electrodes for high-power lithium ion batteries. *Nano Energy* **1**, 518-533 (2012).

11 Cabanas-Polo, S. *et al.* Cyclability of binder-free β-Ni (OH)< sub> 2</sub> anodes shaped by EPD for Li-ion batteries. *Journal of the European Ceramic Society* (2014).

12 Kawamori, M. *et al.* Three-Dimensional Nanoelectrode by Metal Nanowire Nonwoven Clothes. *Nano letters* **14**, 1932-1937 (2014).

13 Li, X., Dhanabalan, A., Bechtold, K. & Wang, C. Binder-free porous core–shell structured Ni/NiO configuration for application of high performance lithium ion batteries. *Electrochemistry Communications* **12**, 1222-1225 (2010).

14 Lee, S.-Y. *et al.* Progress in flexible energy storage and conversion systems, with a focus on cable-type lithium-ion batteries. *Energy & Environmental Science* **6**, 2414-2423 (2013).

15 Balogun, M.-S. *et al.* Binder-free Fe< sub> 2</sub> N Nanoparticles on carbon textile with High power density as novel anode for High-performance flexible lithium ion batteries. *Nano Energy* (2014).

16 Chen, M. *et al.* Porous α-Fe< sub> 2</sub> O< sub> 3</sub> nanorods supported on carbon nanotubes-graphene foam as superior anode for lithium ion batteries. *Nano Energy* **9**, 364-372 (2014).

17 Zhu, L. *et al.* Interconnected carbon nanotube/graphene nanosphere scaffolds as free-standing paper electrode for High-rate and ultra-stable lithium-sulfur batteries. *Nano Energy* (2014).

18 Hwang, T. H., Lee, Y. M., Kong, B.-S., Seo, J.-S. & Choi, J. W. Electrospun core–shell fibers for robust silicon nanoparticle-based lithium ion battery anodes. *Nano letters* **12**, 802-807 (2012).

19 Liu, Y. *et al.* Cycling durability and degradation behavior of La–Mg–Ni–Co-type metal hydride electrodes. *Journal of Alloys and Compounds* **395**, 291-299 (2005).

20 Poizot, P., Laruelle, S., Grugeon, S., Dupont, L. & Tarascon, J. Nano-sized transition-metal oxides as negative-electrode materials for lithium-ion batteries. *Nature* **407**, 496-499 (2000).

21 Xu, W. *et al.* Lithium metal anodes for rechargeable batteries. *Energy & Environmental Science* **7**, 513-537 (2014).

22 Aravindan, V. *et al.* Electrospun NiO nanofibers as high performance anode material for Li-ion batteries. *Journal of Power Sources* **227**, 284-290 (2013).

23 Wang, B., Cheng, J., Wu, Y., Wang, D. & He, D. Electrochemical performance of carbon/Ni composite fibers from electrospinning as anode material for lithium ion batteries. *Journal of Materials Chemistry A* **1**, 1368-1373 (2013).

24 Sun, X. *et al.* Three-Dimensionally "Curved" NiO Nanomembranes as Ultrahigh Rate Capability Anodes for Li-Ion Batteries with Long Cycle Lifetimes. *Advanced Energy Materials* **4** (2014).

25 Sun, X. *et al.* Multifunctional Ni/NiO hybrid nanomembranes as anode materials for high-rate Li-ion batteries. *Nano Energy* **9**, 168-175 (2014).

26 Barakat, N. A., Kim, B. & Kim, H. Y. Production of smooth and pure nickel metal nanofibers by the electrospinning technique: nanofibers possess splendid magnetic properties. *The Journal of Physical Chemistry C* **113**, 531-536 (2008).

27 Kim, C. *et al.* Fabrication of Electrospinning-Derived Carbon Nanofiber Webs for the Anode Material of Lithium-Ion Secondary Batteries. *Advanced Functional Materials* **16**, 2393-2397 (2006).

28 Teo, W. & Ramakrishna, S. A review on electrospinning design and nanofibre assemblies. *Nanotechnology* **17**, R89 (2006).

29 Wu, H., Zhang, R., Liu, X., Lin, D. & Pan, W. Electrospinning of Fe, Co, and Ni nanofibers: synthesis, assembly, and magnetic properties. *Chemistry of materials* **19**, 3506-3511 (2007).

30 Wang, X. *et al.* Nanostructured NiO electrode for high rate Li-ion batteries. *Journal of Materials Chemistry* **21**, 3571-3573 (2011).

31 Laruelle, S. *et al.* On the origin of the extra electrochemical capacity displayed by MO/Li cells at low potential. *Journal of the Electrochemical Society* **149**, A627-A634 (2002).

32 Do, J.-S. & Weng, C.-H. Preparation and characterization of CoO used as anodic material of lithium battery. *Journal of power sources* **146**, 482-486 (2005).

33 Needham, S. A., Wang, G. & Liu, H. K. Synthesis of NiO nanotubes for use as negative electrodes in lithium ion batteries. *Journal of Power Sources* **159**, 254-257 (2006).

34 Li, T., Ni, S., Lv, X., Yang, X. & Duan, S. Preparation of NiO–Ni/natural graphite composite anode for lithium ion batteries. *Journal of Alloys and Compounds* **553**, 167-171 (2013).

35 Su, L., Zhou, Z. & Shen, P. Ni/C hierarchical nanostructures with Ni nanoparticles highly dispersed in N-containing carbon nanosheets: origin of Li storage capacity. *The Journal of Physical Chemistry C* **116**, 23974-23980 (2012).

36 Su, D., Ford, M. & Wang, G. Mesoporous NiO crystals with dominantly exposed {110} reactive facets for ultrafast lithium storage. *Scientific reports* **2** (2012).

37 Li, X., Dhanabalan, A. & Wang, C. Enhanced electrochemical performance of porous NiO–Ni nanocomposite anode for lithium ion batteries. *Journal of Power Sources* **196**, 9625-9630 (2011).

38 Li, D. *et al.* Building Ni3S2 Nanotubes array and Application as an Electrode in Lithium Ion Battery. *Chemical Communications* (2014).

39 Ogihara, N. *et al.* Disordered carbon negative electrode for electrochemical capacitors and high-rate batteries. *Electrochimica acta* **52**, 1713-1720 (2006).

40 Favors, Z. *et al.* Scalable Synthesis of Nano-Silicon from Beach Sand for Long Cycle Life Li-ion Batteries. *Scientific reports* **4** (2014).

41 Zhang, S., Xu, K. & Jow, T. Electrochemical impedance study on the low temperature of Li-ion batteries. *Electrochimica acta* **49**, 1057-1061 (2004).

42 Wang, W. *et al.* Silicon Decorated Cone Shaped Carbon Nanotube Clusters for Lithium Ion Battery Anodes. *Small* (2014).

43 Verma, P., Maire, P. & Novák, P. A review of the features and analyses of the solid electrolyte interphase in Li-ion batteries. *Electrochimica Acta* **55**, 6332-6341 (2010).

3. Lithium Sulfur Batteries

3.1. Advanced Sulfur-Silicon Full Cell Architecture for Lithium Ion Batteries

(See Next Page)

Advanced Sulfur-Silicon Full Cell Architecture for Lithium Ion Batteries

Rachel Ye[1§], Jeffrey Bell[2§], Daisy Patino[2], Kazi Ahmed[3], Mihri Ozkan[3], and Cengiz S. Ozkan[1,2*]*

[1]Mechanical Engineering Department, University of California Riverside, 900 University Ave. Riverside, CA 92521

[2]Material Science and Engineering Program, University of California Riverside, 900 University Ave. Riverside, CA 92521

[3]Electrical and Computer Engineering Department, University of California Riverside, 900 University Ave. Riverside, CA 92521

§ = (Designates equal contributions)

Abstract

Lithium-ion batteries are crucial to the future of energy storage, however the energy density of current lithium-ion batteries are insufficient for future applications. Sulfur cathodes and silicon anodes have garnered a lot of attention in the field due their high capacity potential. Although, recent developments in sulfur and silicon electrodes show

exciting results in half cell formats, but when put together into a full cell format, neither electrode can act as a lithium source. Current methods toward incorporating lithium in sulfur-silicon full cells involves prelithiating silicon or using lithium sulfide. These methods however, complicate materials processing and creates safety hazards. Herein, we present a novel full cell battery architecture that bypasses the issues associated with current methods. This battery architecture gradually integrates controlled amounts of pure lithium into the system by allowing lithium access to the external circuit. We achieved a high specific energy density of 350 Wh/kg after 250 cycles at C/10. This work will open up opportunities for future research into sulfur-silicon full cells.

1.1 Overview

Lithium-ion batteries (LiBs) outperform other battery technologies on the market, making them the choice for consumer electronics and electric vehicles (EVs). However, performance and cost demands have begun exceeding the capabilities of current LiB technology. Researchers have turned towards next generation battery materials to procure cheaper, higher capacity batteries.[1-7]

Current LiBs utilize a cathode made from lithiated metal oxides, such as lithium nickel manganese cobalt oxide (NMC). The cathode is traditionally countered by a graphite anode, although some in the industry have recently started incorporating silicon into the anode (1%-5%). The advantages to this combination are high rate capabilities, low capacity degradation, and long lifetime. The disadvantages are a limited energy density,

with NMC/Graphite having the highest theoretical energy density at 605 Wh/kg, and high cost of $180/kWh. To reduce costs, researchers have turned toward more energy dense and cheaper materials.

Sulfur is an attractive cathode material due to its theoretical capacity of 1675 mAh/g. However, implementation of sulfur has been slow due to its inherent problems including polysulfide shuttling, volumetric expansion, and poor conductivity.[1,2,8-11] Polysulfide shuttling results from higher order polysulfides dissolving in the electrolyte, causing long term capacity degradation and slowing reaction kinetics during runtime.[12] Volumetric expansion results from sulfur expanding (80%) during lithiation/delithiation which causes mechanical degradation to the electrode's conductive network.[12] Finally, sulfur's insulating properties affect the electrode's rate capabilities. Fortunately, researchers have discovered methods to alleviate these issues ranging from mechanical barriers, to porous carbon networks, to other chemical methods.[13-17] Promising performance from these solutions have resulted in much fervor surrounding sulfur.

The current anode of choice is silicon for its high theoretical capacity of 4200 mAh/g. Silicon faces two challenges - poor conductivity, and volumetric expansion.[18-21] During lithiation/delithiation, silicon's volume changes 400% which mechanically pulverizes the electrode, and degrades its cycle life and rate capabilities.[21,22] To alleviate these issues, researchers utilize novel methods including nano silicon structures, conductive additives, and binders.[23-29] Ultimately, the immense focus on solving each electrode's

issues has resulted in less research effort on combining a sulfur cathode and silicon anode in a full-cell configuration.

A full cell using sulfur and silicon electrodes is attractive for several reasons. Sulfur and silicon are environmentally benign and abundant. Furthermore, theoretical energy density of a sulfur silicon full-cell (SSFCs) is 1982 Wh/kg, far exceeding the theoretical energy density of current LiBs while only potentially costing $13/kWh. However, a major restriction for SSFCs is the lithium source. Currently, researchers utilize pre-lithiated materials such as lithium sulfide or lithium silicide, allowing for energy densities up to 600 Wh/kg. However,these full cells suffer from short cycles lives, typically less than 50 cycles, while the material used require specialized equipment and face restrictions in processing.[30-32]

Here, we present an advanced LiB architecture utilizing a sulfur cathode and silicon anode with lithium source integrated into the Si anode that can bypass these issues. The SSFC exhibits an energy density of 350 Wh/kg for 260 cycles at C/10. To the best of our knowledge, an SSFC with this architecture has not been reported.

2.1 Results and Discussion

Electrodes for SSFCs were constructed using a facile process. Shown in Figure 10A, the silicon electrode is patterned to create an access point for the lithium chip, sitting on top of the silicon electrode, to contact the current collector. The access point allows electrons to transfer from lithium to positive terminal, Figure 10B, creating a complete

circuit. The patterned silicon electrode is engineered to expose a small surface area of the current collector, thereby maximizing silicon slurry loading. As a result, only a small surface area of the lithium chip makes direct contact with the current collector.

During discharge, the surface area of the lithium chip with direct access to the outer circuit alongside with the silicon anode should act as a lithium source. This provides lithium ions to the cathode through electrolyte while electrons travel to the cathode through the outer circuit. During charge, due to the reducing property of lithium, lithium ions will preferentially react with the silicon anode instead of the lithium chip. As cycling increases, lithium without direct access to the outer circuit also integrates into the system. This results in an increase in capacity, discussed later in Figure 5C. Each SSFC requires roughly 6.44 mg of lithium, accounting for the lithiation of sulfur and silicon, along with consumption of lithium by the SEI. (See supplementary document for detailed calculation) To ensure enough lithium is available in the system, each cell is loaded with 8 mg of lithium.

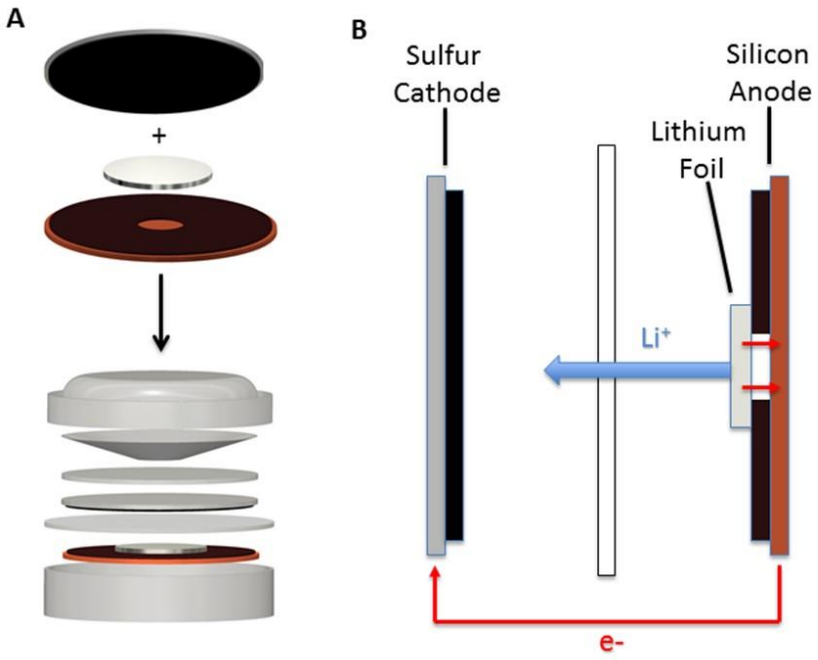

Figure 10. A) Advanced battery architecture with lithium placed in circuit on-top of the silicon electrode. B) Cross sectional discharge schematic of SSFC.

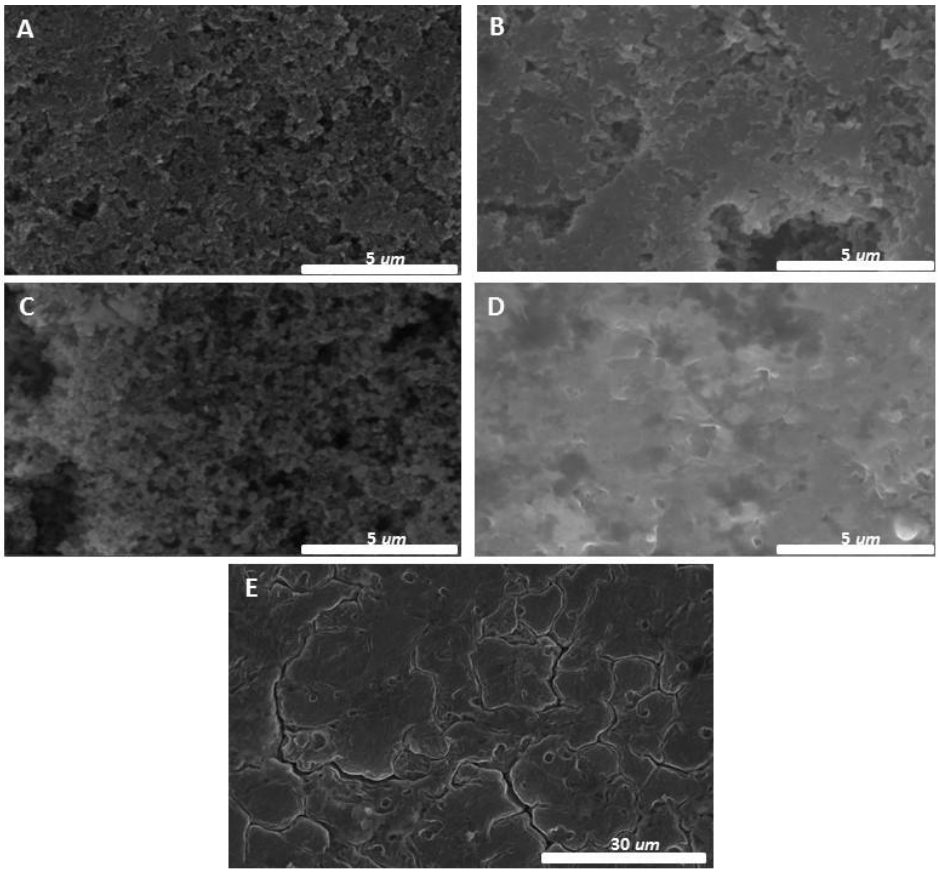

Figure 11. A) Pre-cycling SEM imaging of sulfur electrode for SSFC. B) Post-cycling SEM imaging of sulfur electrode for SSFC at 310 cycles. C) Pre-cycling SEM imaging of silicon electrode for SSFC. D) Post-cycling SEM imaging of silicon electrode for SSFC at 310 cycles. E) Post-cycling SEM imaging of lithium foil for SSFC at 310 cycles.

The morphology of the electrodes was examined using SEM, shown in Figure 11. Figure 11A and 11C show the surface of the sulfur and silicon electrodes respectively before they were cycled in the SSFC. Figure 11B and 11D show the post-cycling morphology of

the corresponding electrodes. Pre-cycling SEM shows the electrode materials are loosely packed with large void spaces existing after calendaring. Post-cycling SEM shows less void space due to the volumetric expansion of active materials and the formation of SEI products during lithiation.[3,18] Figure 11E shows the post-cycling SEM of the lithium foil after 310 cycles. Since the SSFC is not utilizing any dendrite suppression technique, dendrites should start to form on the foil as early as 20 cycles if the lithium is being used as the anode. The lack of dendrite formation in Figure 11E suggested that the foil was only used as the source of lithium rather than the anode.

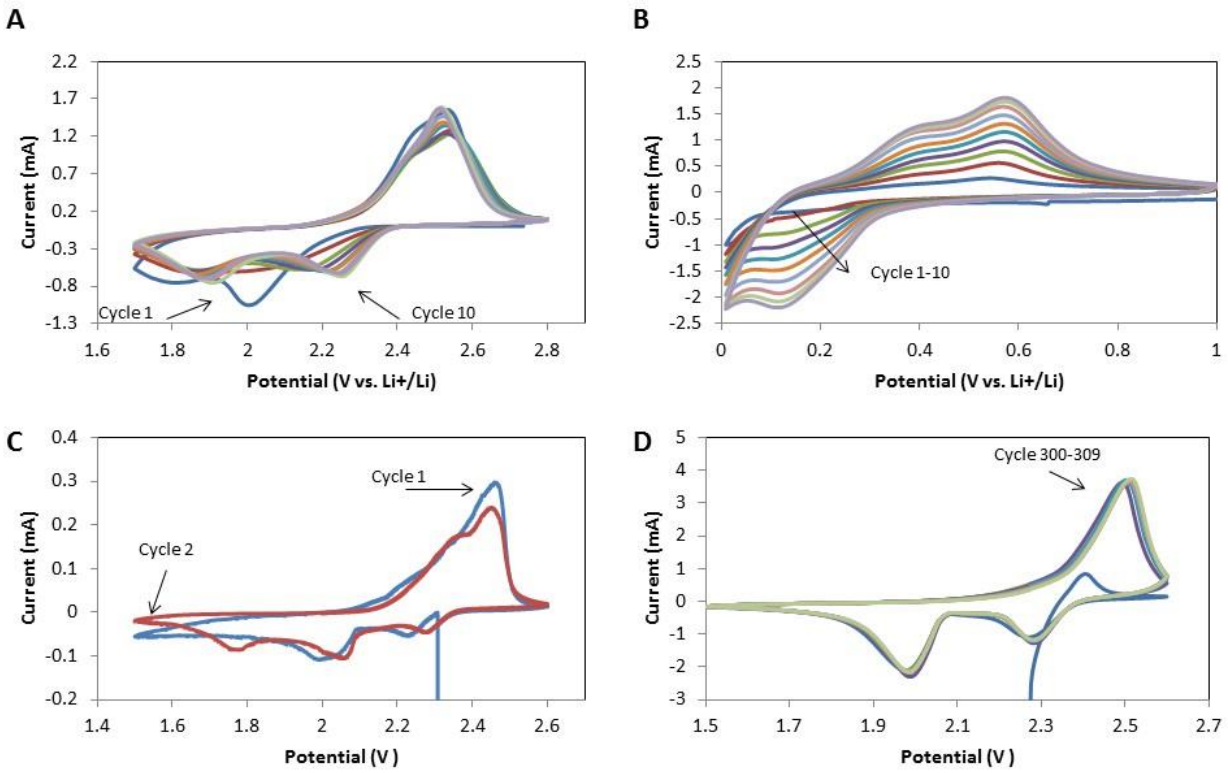

Figure 12. A) Cycles 1-10 for the sulfur electrode at a scan rate of 0.1 mVs^{-1}.B) Cycles 1-10 for the silicon electrode at a scan rate of 0.1 mVs^{-1}. C) CV of Cycles 1-2 for the SSFC at a scan rate of 0.05 mVs^{-1}. D) CV of Cycles 300-309 for the SSFC at a scan rate of 0.1 mVs^{-1}.

CV was performed at a scan rate of 0.1 mV s^{-1} over cycles 1-10 for both sulfur and silicon half-cells. SSFC CV was conducted at 0.05 mV s^{-1} and 0.1 mV s^{-1} respectively for cycles 1-

2 and 300-309. The 0.05 mV s^{-1} scan rate was used to accommodate the aforementioned requirements for lithium integration during cycles 1-2. Figures 3A and 3B show CV profiles for cycles 1-10 of sulfur and silicon half-cells respectively. Shown in Figure 12A, the sulfur half-cell exhibits typical characteristics of chemical reactions between sulfur and lithium ions with two cathodic peaks at 1.9 V and 2.25 V followed by an anodic peak at around 2.5 V.[33,34] The notable difference for cycles 1 and 2 is the offset peaks at 1.8 V and 2 V. Peaks shifting towards a higher potential indicates a higher ionic conductivity stemming from increased polysulfides and SEI formation.[35] Shown in Figure 12B, the silicon half-cell shows typical cathodic peaks at 0.18 V and 0.1 V with anodic peaks at 0.4 V and 0.6 V. The peaks corresponding to lithiation/delithiation increase in intensity over time, resulting from lithiation of the native SiO_2 layer and lithium gaining access to additional silicon.[36] The peak associated with SEI formation (0.67 V) does not exist after the first cycle, showing bulk SEI formation has been achieved.[36]

Figures 3C and 3D show CV profiles for the SSFC for cycles 1-2 and 300-309 respectively. Figures 3C and 3D exhibit a similar electrochemistry to Figure 12A resulting from interactions between lithium ions and sulfur dominating the SSFC chemistry. In Figure 12C, the first cycle has cathodic peaks at 2 V and 2.2 V resulting from limited amounts of lithium participating in the first discharge. Cycle two has an additional peak around 1.8 V, which we hypothesize to be a result of the negative voltage potential between the non-participating lithium and silicon. The resulting equilibrium voltage equals to the difference between the original potential of unlithiated sulfur and lithium (~2.8 V), and

the potential between silicon and lithium (~1V). The extra anodic peak at 2.35V is also caused by non-participating lithium. This causes a negative potential between lithium and silicon (~0.15 V), shifting the normal peak at 2.5 V down to 2.35 V.

Figure 12D shows the CV profile for the SSFC once it has reached equilibrium. The two cathodic peaks at 2.0 V and 2.3 V followed by an anodic peak at 2.5 V match the electrochemistry of sulfur half-cell, Figure 12A. This slight shift in peaks towards a higher potential represents complete activation of the lithium and further kinetic enhancement of the system.[35] The difference in current range between Figure 12C and Figure 12D is attributed to a change in the peak current, alluding to a higher capacity and reactivity.[37] This coincides with the increase in capacity as seen in Figure 14C.

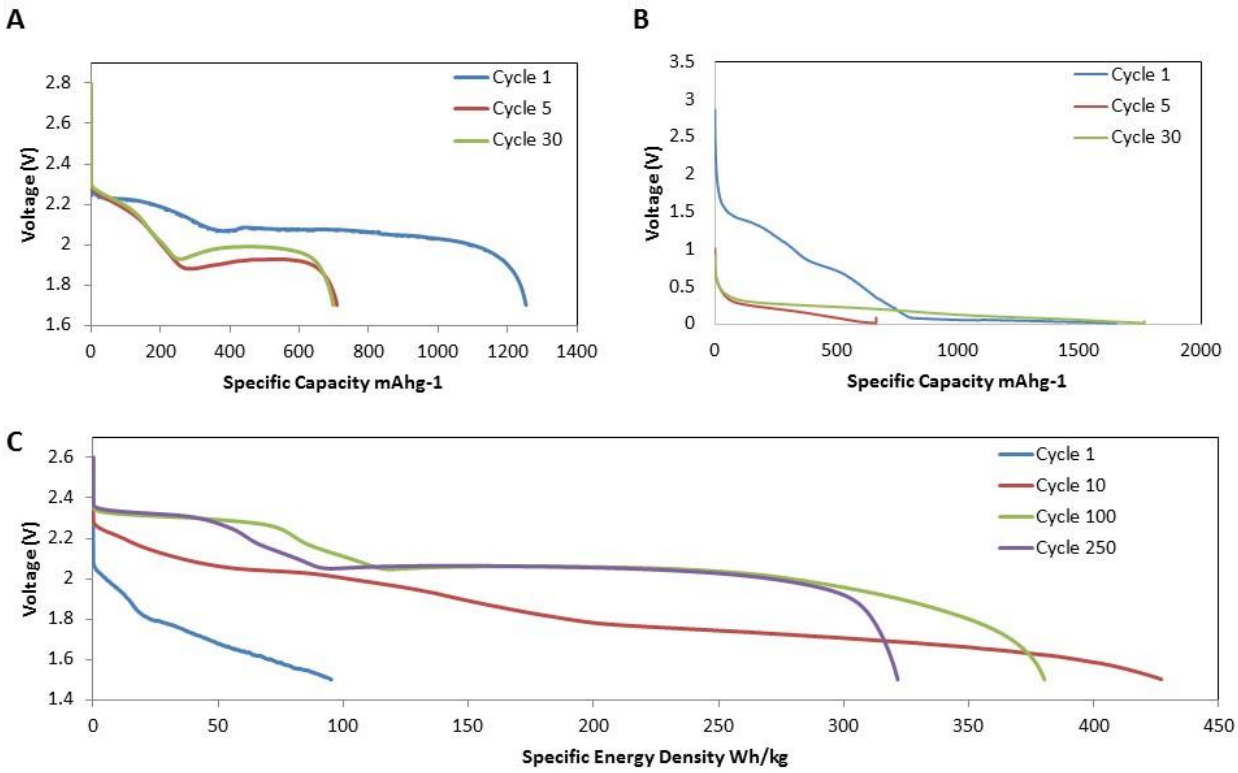

Figure 13. A) Galvanostatic voltage profiles for the sulfur electrode at C/10 for selected cycles. B) Galvanostatic voltage profiles for the silicon electrode at C/10 for selected cycles. C) Galvanostatic voltage profiles for the SSFC at C/10 for selected cycles.

The charge-discharge profiles for the SSFC, sulfur and silicon cells are shown in Figure 13. The potential of the sulfur half-cell during its first discharge in Figure 13A exhibits two long plateaus at 2.3 V and 2.1 V. The first long plateau at 2.3 V is associated with

long chain polysulfide formation (Li_2S_X:x=8,6,4).[38] The second plateau at 2.1 V corresponds to the formation of Li_2S_2 and Li_2S.[38,39] After the first cycle, the plateau at 2.1 V shifts to 1.9 V due to the enhanced kinetics, which concurs with the CV profile in Figure 12A. The potential of the silicon half-cell during its first discharge in Figure 13B exhibits a long plateau starting at 1.4 V. This corresponds to the formation of the solid electrolyte interphase.[24,40] The voltage plateau at 1.4 V disappears after the first cycle, and is replaced with a plateau at 0.2 V. This is in accordance with the cathodic peak seen in Figure 12B. The CV and discharge profiles for the sulfur and silicon half-cells are also consistent with data reported in literature.[3,29]

Figure 13C shows the discharge profile for the SSFC. The first cycle has plateaus at 2 V and 1.8 V which concur with Figure 12C. At cycle 2, an excess plateau at 1.8 V results from the aforementioned equilibrium potential between sulfur, silicon, and non-participating lithium. This speculation is further proven by the change of the 1.8V plateau, which becomes shorter as the test progresses, indicating less non-participating lithium. The voltage difference between the 10th and 100th cycles results from the cell conditioning and stabilizing by incorporating additional lithium over time. Once all the available lithium participates in the battery system, as shown in cycle 100 and 250, the voltage profile of the SSFC is in accordance with the sulfur half-cell. This proves that a stabilized SSFC act similar to a conventional full cell where cathode dominates the electrochemistry.[30,31]

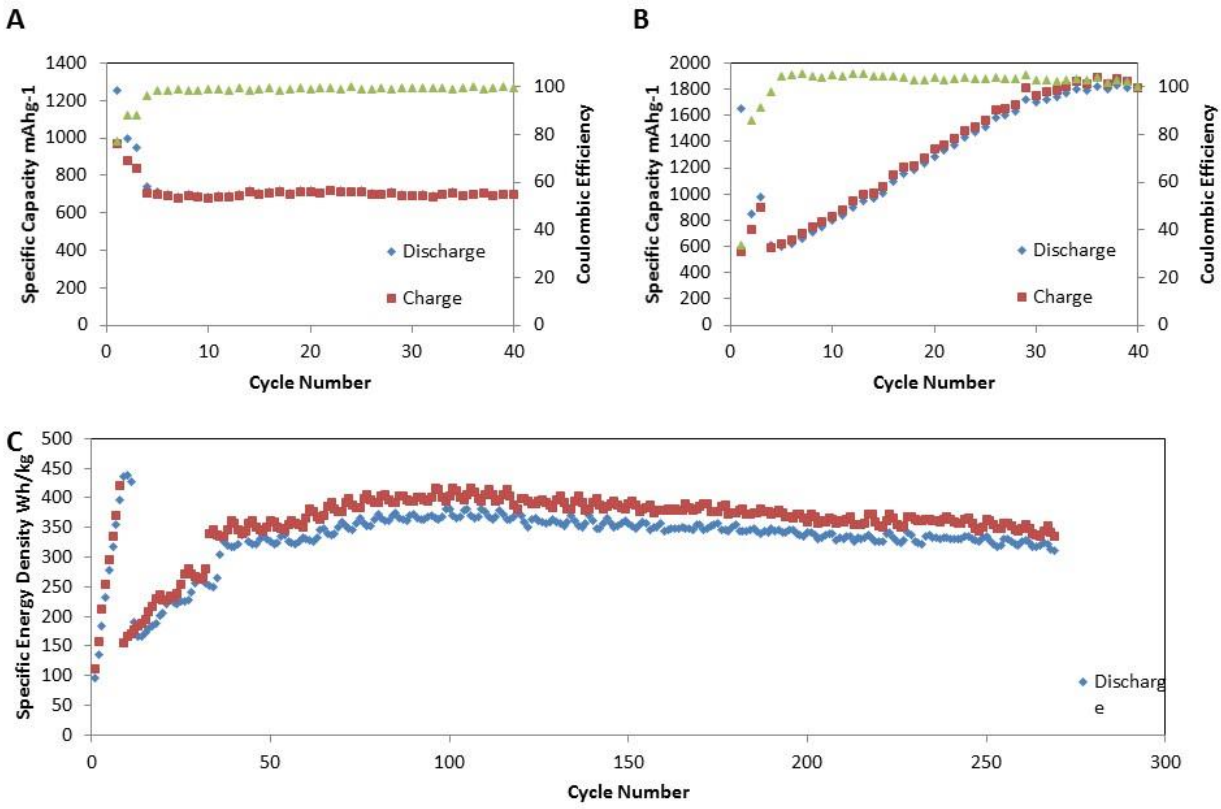

Figure 14. A) Galvanostic cycling of the sulfur electrode at C/10 for 40 cycles. B) Galvanostic cycling of the silicon electrode at C/10 for 40 cycles.) Deep Galvanostic cycling of the SSFC at C/10 for more than 250 cycles.

Galvanostatic cycling of the sulfur and the silicon half-cell was carried out at a potential window of 1.7–2.8 V and 0.01-1 V respectively. In Figure 14, the capacity for the batteries was measured at a rate of C/10 after being conditioned at C/50 for 3 cycles.

The sudden decrease in performance at cycle 4 for both of the half cells is due to the rate change from C/50 to C/10. In Figure 14A, the sulfur half-cell has an initial capacity of 1254 $mAhg^{-1}$ and maintains a capacity of 700 $mAhg^{-1}$ for 40 cycles with a coulombic efficiency greater than 99%. The decrease in capacity is attributed to SEI formation, polysulfide shuttling, as well as mechanical degradation of the electrode. In Figure 14B, the silicon half-cell has an initial capacity of 600 $mAhg^{-1}$, and stabilizes at 1800 $mAhg^{-1}$ within 40 cycles with a coulombic efficiency greater than 99%. The increase in capacity is attributed to the calendared electrode limiting the expansion of lithiated silicon and electrolyte penetration.[38] This coincides with Figure 12B, wherein the overall CV curve of the silicon half-cell increases in intensity over time, alluding to a higher capacity.[37]

Figure 14C shows galvanostatic cycling for the SSFC. The energy density of the SSFC, which is calculated based on the total anode and cathode weight (see supplementary information for details), is recorded for 250 cycles. The wave like fluctuations in capacity results from temperature changes occurring inside the testing room. The initial energy density of the SSFC is 100 Wh/kg at C/50 then increases to 414 Wh/kg over 10 cycles. The sudden drop in capacity at cycle 11 is due to the current rate change from C/50 to C/10. The increase in energy density is attributed to the continuous integration of non-participating lithium, shown in Figure 14C; this hypothesis is confirmed by Figures 3, 4, and 7. The SSFC has an energy density of 350 Wh/kg for over 250 cycles and a coulombic efficiency of approximately 95%. The fluctuation in coulombic efficiency from cycle 1 to 150 is due to the process of lithium integration, which creates a unique chemical

reaction to the SSFC. When charging a conventional full-cell, lithium ions from the cathode travels to the anode while electrons travels through the outer circuit from cathode to anode as well, as a result, the anode materials are lithiated. Li-ions and the electrons are then returned to the cathode during discharge. In the SSFC, lithium starts on the anode side, thus discharge happens during the first cycle. We propose that during discharge, lithium ions from the lithium chip travel to the cathode through electrolyte, while the electrons from the lithium chip travels through its contact point with the current collector and joins the electrochemistry process. However, in later cycles, lithium that is not directly in contact with the current collector can only join the system by either transferring electrons through the relatively insulating silicon slurry or by lithiating the silicon slurry during charge. This additional lithiation increases the charge capacity, which in turns decreases the coulombic efficiency. Hence, the coulombic efficiency of cycles 1 to 150 are low and unstable despite the cathode operates with a stable coulombic efficiency of 99%, shown in Figure 14A. After 150 cycles all required lithium is incorporated into the SSFC system and is actively participating in the redox reaction, however, excess lithium remains. During charge, lithium ions from the cathode plate onto the excess lithium chip while in parallel, lithium ions from the chip react with the silicon anode. As a result, the coulombic efficiency after 150 cycles have improved but are still in the range of 95% instead of being similar to the sulfur half-cell.

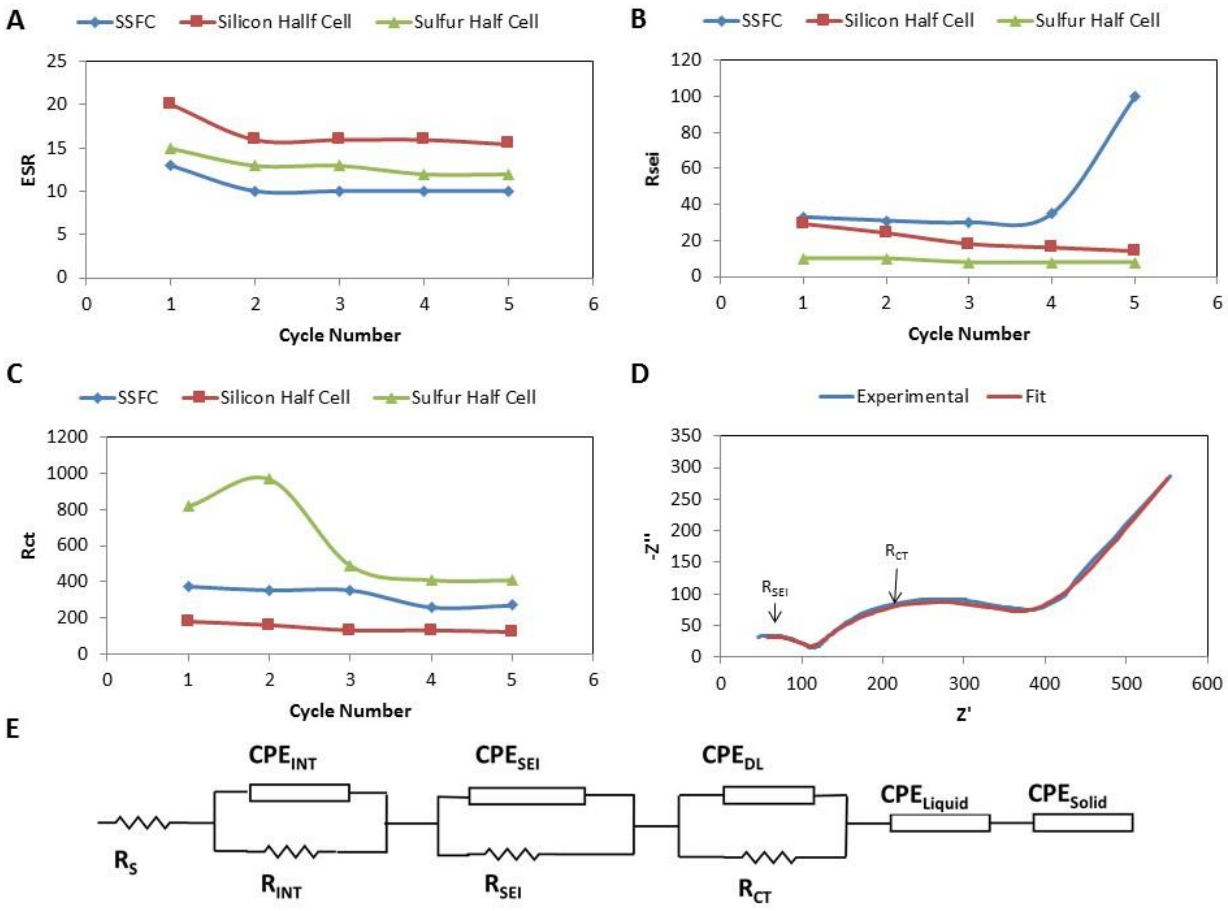

Figure 15. Impedance parameters during initial cycles for SSFC, silicon half-cell, and sulfur half-cell. A) ESR. B) R_{CT}. C) R_{SEI}. D) Experimental data SSFC cycle. 5 E) EEC used to obtain parameters.

Electrochemical impedance spectroscopy, shown in Figure 15, is a non-destructive method allowing us to investigate the integrity of electrode-electrolyte interface,

passivation layers, electronic conductivity of electrode material, diffusion of lithium within electrode, and diffusion of lithium ions in electrolyte near electrode surface. Potentiostatic EIS is utilized to characterize the cells' complex impedance by measuring the current response to a small sinusoidal voltage signal. Impedance is obtained for a selected number of frequency points between the bounds of 10 kHz and 10 mHz.

Figure 15E shows the electrical equivalent circuit used to model the impedance of lithium-ion cells at a fully charged state. A fit between the impedance response of the circuit and that of the cell is obtained by tuning the circuit parameter values. The constant phase elements (CPE) present in the circuit are capacitances that are spatially non-uniform. Equation 1 gives the formula used to calculate the impedance of CPE. Here Q is analogue to capacitance, and n is an ideality factor that is constrained between 0 and 1, while an ideality factor of 1 is identical to an ideal capacitor.

$$Z_{CPE} = \frac{1}{Q(j\omega)^n} \qquad (1)$$

In Figure 15E, the value of equivalent series resistance (ESR) represents electrolyte conductivity. R_{INT} quantizes electronic conductivity within electrode matrix, while CPE_{INT} is a measure of the non-ideal capacitance that arises due to this finite conductivity.

CPE_{FILM} and R_{FILM} quantize non-ideal capacitance and resistance associated with the passivating layers. CPE_{DL} measures the nature of the Helmholtz double-layer formed about the electrode-electrolyte interface, while R_{CT} determines the exchange current density. R_{CT} is an indicator of how facile electron exchange kinetics are at the interface. CPE_{LIQUID} quantizes diffusion of lithium ions in electrolyte near electrode surface. This diffusion impedance originates from the concentration gradient of lithium ions existing between the diffuse layer of charge and bulk electrolyte. CPE_{SOLID} represents solid state diffusion of lithium atoms within the electrode material after lithiation and before delithiation.

Figure 15A shows the evolution of ESR during initial cycling in the SSFC and the sulfur/silicon half-cells. ESR in all three cells show a stabilizing trend, which provides evidence of electrochemical durability. It is observed that the two half-cells show a larger ESR than the SSFC. A previous study has shown that electrolyte decomposition is worse in half-cells due to the presence of lithium-metal counter electrodes.[39] Figure 15C shows the change in R_{CT} during the initial cycles in the same cells. It provides evidence for sulfur having slower kinetics than silicon. All three cells show a stabilizing trend over the initial cycles.

Figure 15B shows how R_{SEI} changes for the three cells within the same cycling window. Here we observe that the SSFC has the highest resistance value when compared to silicon and sulfur half-cells. We propose that the method we utilized to lithiate the full-

cell assembly contributed to this observation. Lithium metal placed within the SSFC formed its own SEI during the initial cycling while the lithium content was slowly integrated into the anode. While the chip lost its lithium content to silicon anode, the SEI layer formed on top of it remained. Additionally, another SEI layer formed on the silicon anode as it participated in active lithiation/delithiation reactions. Thus, SSFC exhibits SEI impedance that originate from the silicon anode, from conductive carbon added in sulfur cathode, and from the lithium metal itself used to lithiate the full-cell. We also observe a spike in R_{SEI} at the end of the 5th cycle. We hypothesize that this spike occurs due to the majority of SEI formation taking place on the silicon anode. We also observed that sulfur half-cell showed the lowest R_{SEI} value among the three cells. This is so because sulfur does not natively form any permanent passivation film similar to SEI layers observed in silicon or carbon electrodes. SEI impedance observed in our sulfur electrodes originate from the carbon additive added to the electrode matrix as conductive agent.

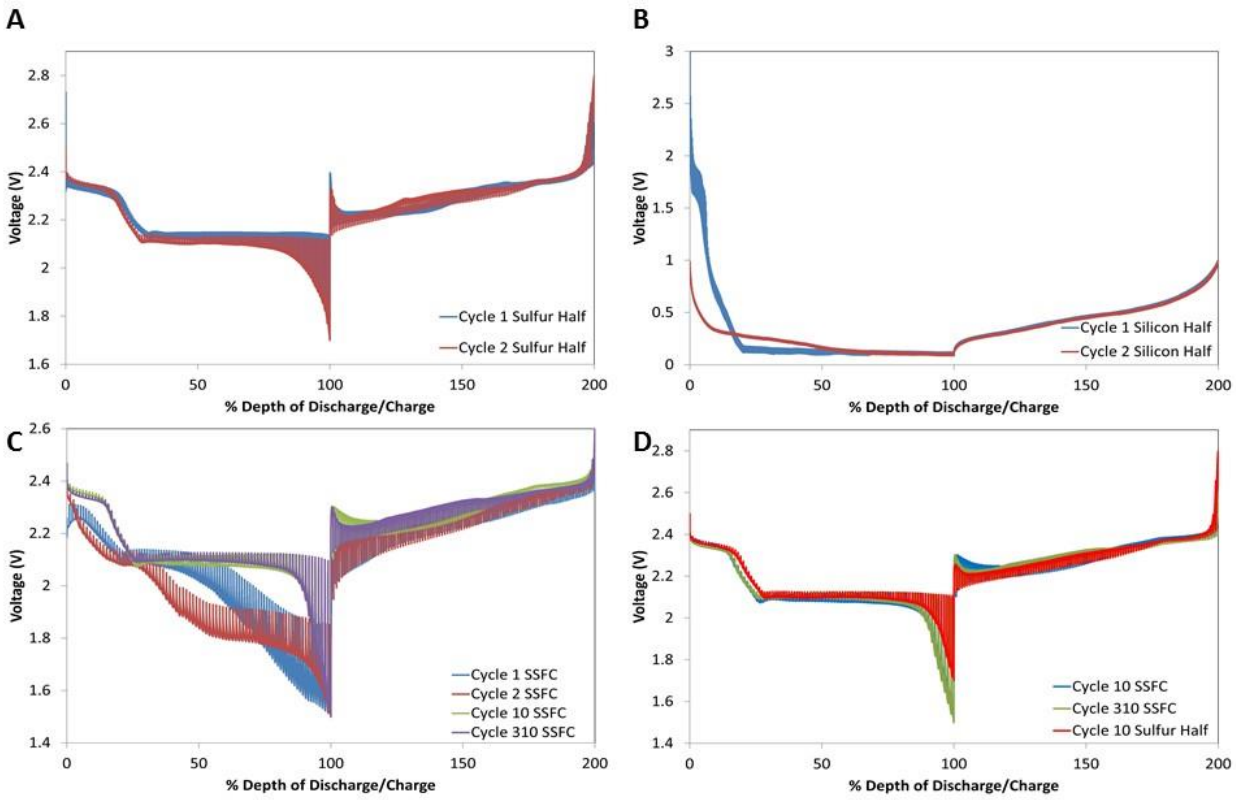

Figure 16. A) GITT analysis on the sulfur electrode at C/50 with 10 minutes rest for cycles 1-2. B).GITT analysis on the silicon electrode at C/50 with 10 minutes rest for cycles 1-2. C) GITT analysis on the SSFC at C/50 with 10 minutes rest for cycles 1, 2, 10, 310. D) GITT analysis comparing sulfur electrode at cycle 10 vs SSFC at cycles 10,310.

GITT, shown in Figure 16, was employed to investigate changes in lithium diffusivity within the individual battery systems.[43,44] The batteries were subjected to current pulse intervals with a rate of C/50 for 10 minutes, followed by 10 minute rests until complete discharge/charge. In Figure 16, the varying thickness of the voltage profiles represent varying lithium diffusivities in the system. Thinner voltage profiles indicate improved diffusivity while thicker voltage profiles represent the inverse.[45,46]

In Figure 16A, the profile for the sulfur half-cell displays a slight decrease in voltage plateaus from cycles 1 to 2. This occurrence is also observed in Figure 12A & 12A, and is attributed to the change in ionic and electric conductivity caused by the incremental SEI formation and polysulfide shuttling.[40] As seen in Figure 16B, the silicon half-cell experiences a voltage shift within the first two cycles; this is attributed to SEI formation, coinciding with Figure 13B. However, voltage profiles and diffusivity equilibrate by the second cycle, indicating that the silicon half-cell has faster kinetics than the sulfur half-cell as inferred by Figure 15C. Hence, it is determined that the kinetics of sulfur half-cell is the limiting factor for the diffusivity of the SSFC.

Figure 16C shows the GITT profile for the SSFC. Figure 16C depicts the voltage profiles of the SSFC resembling the sulfur half-cell, revealing plateaus at 2.3 V and 2.1 V after reaching equilibrium. However, the first cycle of the SSFC shows a discharge profile offset from the sulfur half-cell; this is attributed to limited lithium participation in the first cycle. The excess voltage plateau in cycle 2, at roughly starting at 50% depth of

discharge, alludes to the Li incorporation issues associated with the architecture of the cell. The broad voltage fluctuation in cycles 1-2's GITT profile indicate a nonuniform material utilization caused by part of the electrode not being lithiated with the limited participating lithium, supporting the aforementioned speculation. At cycle 10, the voltage profile of SSFC already resembles a sulfur half-cell. The observable change in diffusion in cycle 2 to 10 is a result of total lithium utilization allowable in the system. This change in the voltage profile comparing to normal cycling, figure 13C, is due to the pulsed discharge currents of GITT progressing the cell at a faster rate allowing complete lithium integration by cycle 10. Once reaching complete lithium utilization, the diffusivity of the system continue to improve from cycles 10 to 310. Thinner voltage profiles as well as a higher voltage plateau are observed in the subsequent cycles, which is a result of enhanced kinetics.

Figure 16D compares the diffusivity of SSFC to the sulfur half-cell, wherein we see a notable difference within the early cycles. At 80 - 100% depth of discharge, the observable difference in diffusivity from the half-cell to SSFC is caused by the charge transfer resistance of the silicon anode. Similarly, once the cell starts to charge, the notable difference in diffusivity profiles at 0-20% depth of charge is a result of charge transfer resistance in the cathode for the SSFC. Ultimately, Figure 16D depicts the SSFC voltage profile continues to coincide with that of the half-cell once it has developed a complete utilization of lithium.

3.1 Conclusion

Herein, we have presented a simple alternative to prelithiated sulfur-silicon full cell systems by allowing lithium access to the external circuit. In addition, this method allows for the controlled loading of lithium to compensate for SEI formation and lithium degradation. As a new full cell configuration for next generation lithium ion batteries, the SSFC demonstrates an energy density of 350 Wh/kg over 250 cycles at C/10. Furthermore, this is the first time, to the best of our knowledge, a sulfur silicon full cell has been fully characterized using EIS, CV and GITT. The results presented will pave the way for new research into sulfur and silicon full cells.

4.1 Experimental Details

4.2 Material Synthesis

The SSFCs consist of a sulfur cathode and a silicon anode. The sulfur cathode was made with 20 wt% Poly(acrylic acid) (PAA, 1800 g/mol,Sigma-Aldrich) and 80% wt% acetylene black sulfur composite(ABS). The aforementioned ABS was made by dissolving 200 mg of Sulfur (S, 99.998% trace metals basis, Sigma-Aldrich) in 20 ml of Dimethyl Sulfoxide (DMSO, Fisher Chemical) at 90 C, heated by a heating jacket (Brisk Heat). 129 mg of Acetylene black (Alfa aesar, 50% compressed) was then added to the solution, the solution was stirred for 3 hours before the heating jacket was removed and the solution was allowed to cool while stirring. The resulting ABS composite was then washed by anhydrous ethanol (Decon Labs, Inc.) several times to ensure the removal of DMSO and

dried at 60C for 24 hours. To make the sulfur electrode, Poly(acrylic acid) (Sigma Aldrich, 450,000) and ABS were mixed with 1-Methyl-2-pyrrolidinone (NMP, Sigma-Aldrich) and then casted on a large piece of aluminum chip (Alfa Aesar, 0.025mm thickness, 99.45% purity) by a doctor blade (MTI Automatic Thick Film Coater, BYK Doctor Blade). The casted electrode sheet was then dried in a convection oven (Cole-Parmer, Stable Temp) at 60C for 24 hours. The silicon electrode was made with 40 wt% of commercial silicon (GNM Silicon nanoparticles 80nm), 25 wt% Acetylene black (Alfa aesar, 50% compressed), and 35 wt% Poly (acrylic acid) (Sigma Aldrich, 450,000). The materials were mixed and sonicated in ethanol and then casted on a large copper chip (Alfa Aesar, 0.025mm thickness, 99.8% purity) with a doctor blade (BYK) and was then dried at 60C for 24 hours**.** Both electrodes were calendared with a 0.04 mm calendar gap using a calendaring machine (IRM) before being constructed into a coin cell.

4.3 Physical Characterization

The morphology of the electrode pre and post cycling was observed by scanning electron microscopy (NovaNanoSEM 450).

4.4 Electrochemical Characterization

To make the SSFC battery, a silicon electrode (16mm in diameter) was first put inside a negative cap (MTI type 2032 coin cell case) and a piece of lithium (MTI Lithium Chip 15.6

Dia x 0.25t mm) with corresponding weight (4-6 mg depending on electrode weight, with adjustments for SEI consumption) was adhered to the top of the silicon electrode inside an Ar filled glovebox (H2O < 0.5 ppm, O2 < 0.2 ppm, Vacuum Atmosphere Co.) to form a complete circuit. The amount of lithium needed was calculated based on the electrode weights and SEI lithium consumption of the half-cells. Next, separators (Celgard 25um 3501) of various sizes were placed on top to prevent any possibility of shorting. Sulfur electrode (16mm in diameter) was then placed on top followed by two spacers, a spring, and the positive cap were added with the electrolyte in between (1:1 DOL:DME, 1wt%$LiNO_3$, 1M LiTFSI). The battery was then sealed using a battery crimper (MTI, MSK-160D). The battery was tested under room temperature with a Bio Logic (BCS 810 Testing Module) using different testing methods, including Galvanostatic Cycling with Potential Limitation (GCPL), Cyclic Voltammetry (CV), Potentiostatic Electrochemical Impedance Spectroscopy (PEIS) and Galvanostatic Intermittent Titration Technique (GITT) in voltage window ranging from 1.5V to 2.6V. The same tests were also performed for the sulfur half-cell (between 1.7V to 2.8V) and the silicon half-cell (between 0.01V to 1V). The Sulfur weight percentage in the Acetylene Black Sulfur composite (ABS) was measured using thermogravimetric analysis (TGA), showing 57% weight sulfur. The SSFC and sulfur half-cell were conditioned with a current rate of 0.175 mA (C/50), and cycled at 0.875 mA (C/10). The silicon half-cell was conditioned at a current rate of 0.336mA (C/50), and cycled at 1.68 mA (C/10).

References

1 Yin, Y. X., Xin, S., Guo, Y. G. & Wan, L. J. Lithium–sulfur batteries: electrochemistry, materials, and prospects. *Angewandte Chemie International Edition* **52**, 13186-13200 (2013).

2 Choi, N. S. *et al.* Challenges Facing Lithium Batteries and Electrical Double-Layer Capacitors. *Angewandte Chemie International Edition* **51**, 9994-10024 (2012).

3 Zhao, X. *et al.* Lithium/Sulfur Secondary Batteries: A Review. *JOURNAL OF ELECTROCHEMICAL SCIENCE AND TECHNOLOGY* **7**, 97-114 (2016).

4 Scrosati, B. Recent advances in lithium ion battery materials. *Electrochimica Acta* **45**, 2461-2466 (2000).

5 Tarascon, J.-M. & Armand, M. Issues and challenges facing rechargeable lithium batteries. *Nature* **414**, 359-367 (2001).

6 Lu, L., Han, X., Li, J., Hua, J. & Ouyang, M. A review on the key issues for lithium-ion battery management in electric vehicles. *Journal of power sources* **226**, 272-288 (2013).

7 Barré, A. *et al.* A review on lithium-ion battery ageing mechanisms and estimations for automotive applications. *Journal of Power Sources* **241**, 680-689 (2013).

8 Park, H., Koh, H. S. & Siegel, D. J. First-Principles Study of Redox End Members in Lithium–Sulfur Batteries. *The Journal of Physical Chemistry C* **119**, 4675-4683 (2015).

9 Wu, F. *et al.* Lithium iodide as a promising electrolyte additive for lithium–sulfur batteries: mechanisms of performance enhancement. *Advanced Materials* **27**, 101-108 (2015).

10 Zhang, S. S. Liquid electrolyte lithium/sulfur battery: fundamental chemistry, problems, and solutions. *Journal of Power Sources* **231**, 153-162 (2013).

11 Manthiram, A., Fu, Y. & Su, Y.-S. Challenges and prospects of lithium–sulfur batteries. *Accounts of chemical research* **46**, 1125-1134 (2012).

12 Canas, N. A. *et al.* Investigations of lithium–sulfur batteries using electrochemical impedance spectroscopy. *Electrochimica Acta* **97**, 42-51 (2013).

13 Pang, Q., Liang, X., Kwok, C. Y. & Nazar, L. F. Advances in lithium–sulfur batteries based on multifunctional cathodes and electrolytes. *Nature Energy* **1**, 16132 (2016).

14 Li, Z., Zhang, J. & Lou, X. W. D. Hollow Carbon Nanofibers Filled with MnO2 Nanosheets as Efficient Sulfur Hosts for Lithium–Sulfur Batteries. *Angewandte Chemie International Edition* **54**, 12886-12890 (2015).

15 Shan, J. *et al.* Graphene-directed two-dimensional porous carbon frameworks for high-performance lithium–sulfur battery cathodes. *Journal of Materials Chemistry A* **4**, 314-320 (2016).

16 Balach, J. *et al.* Functional Mesoporous Carbon-Coated Separator for Long-Life, High-Energy Lithium–Sulfur Batteries. *Advanced Functional Materials* **25**, 5285-5291 (2015).

17 Zhang, L. *et al.* Electronic structure and chemical bonding of a graphene oxide–sulfur nanocomposite for use in superior performance lithium–sulfur cells. *Physical Chemistry Chemical Physics* **14**, 13670-13675 (2012).

18 Su, X. *et al.* Silicon-based nanomaterials for lithium-ion batteries: a review. *Advanced Energy Materials* **4** (2014).

19 Zhang, W.-J. A review of the electrochemical performance of alloy anodes for lithium-ion batteries. *Journal of Power Sources* **196**, 13-24 (2011).

20 McDowell, M. T., Lee, S. W., Nix, W. D. & Cui, Y. 25th Anniversary Article: Understanding the Lithiation of Silicon and Other Alloying Anodes for Lithium-Ion Batteries. *Advanced Materials* **25**, 4966-4985 (2013).

21 Liang, B., Liu, Y. & Xu, Y. Silicon-based materials as high capacity anodes for next generation lithium ion batteries. *Journal of Power sources* **267**, 469-490 (2014).

22 Chan, C. K., Ruffo, R., Hong, S. S. & Cui, Y. Surface chemistry and morphology of the solid electrolyte interphase on silicon nanowire lithium-ion battery anodes. *Journal of Power Sources* **189**, 1132-1140 (2009).

23 Wu, H. *et al.* Engineering empty space between Si nanoparticles for lithium-ion battery anodes. *Nano letters* **12**, 904-909 (2012).

24 Favors, Z. *et al.* Stable Cycling of SiO2 Nanotubes as High-Performance Anodes for Lithium-Ion Batteries. *Scientific reports* **4** (2014).

25 Teki, R. *et al.* Nanostructured silicon anodes for lithium ion rechargeable batteries. *Small* **5**, 2236-2242 (2009).

26 Li, X. *et al.* Mesoporous silicon sponge as an anti-pulverization structure for high-performance lithium-ion battery anodes. *Nature communications* **5** (2014).

27 He, Y., Yu, X., Wang, Y., Li, H. & Huang, X. Alumina-Coated Patterned Amorphous Silicon as the Anode for a Lithium-Ion Battery with High Coulombic Efficiency. *Advanced Materials* **23**, 4938-4941 (2011).

28 Kim, H., Han, B., Choo, J. & Cho, J. Three-dimensional porous silicon particles for use in high-performance lithium secondary batteries. *Angewandte Chemie* **120**, 10305-10308 (2008).

29 Li, C. *et al.* Silicon Derived from Glass Bottles as Anode Materials for Lithium Ion Full Cell Batteries. *Scientific Reports* **7**, 917 (2017).

30 Yang, Y. *et al.* New nanostructured Li2S/silicon rechargeable battery with high specific energy. *Nano letters* **10**, 1486-1491 (2010).

31 Hassoun, J. *et al.* A contribution to the progress of high energy batteries: A metal-free, lithium-ion, silicon–sulfur battery. *Journal of Power Sources* **202**, 308-313 (2012).

32 Liu, N., Hu, L., McDowell, M. T., Jackson, A. & Cui, Y. Prelithiated silicon nanowires as an anode for lithium ion batteries. *Acs Nano* **5**, 6487-6493 (2011).

33 Zhang, S. S. Role of LiNO 3 in rechargeable lithium/sulfur battery. *Electrochimica Acta* **70**, 344-348 (2012).

34 Cai, K., Song, M.-K., Cairns, E. J. & Zhang, Y. Nanostructured Li2S–C composites as cathode material for high-energy lithium/sulfur batteries. *Nano letters* **12**, 6474-6479 (2012).

35 Ji, L. *et al.* Porous carbon nanofiber–sulfur composite electrodes for lithium/sulfur cells. *Energy & Environmental Science* **4**, 5053-5059 (2011).

36 Favors, Z. *et al.* Scalable Synthesis of Nano-Silicon from Beach Sand for Long Cycle Life Li-ion Batteries. *Scientific reports* **4** (2014).

37 Bell, J. *et al.* Free-standing Ni–NiO nanofiber cloth anode for high capacity and high rate Li-ion batteries. *Nano Energy* **18**, 47-56 (2015).

38 Vlad, A. *et al.* Roll up nanowire battery from silicon chips. *Proceedings of the National Academy of Sciences* **109**, 15168-15173 (2012).

39 Delpuech, N. *et al.* Mechanism of Silicon Electrode Aging upon Cycling in Full Lithium-Ion Batteries. *ChemSusChem* (2016).

40 Busche, M. R. *et al.* Systematical electrochemical study on the parasitic shuttle-effect in lithium-sulfur-cells at different temperatures and different rates. *Journal of Power Sources* **259**, 289-299 (2014).

3.1.1 Supplementary Information

Cost calculation

According to data found online the cost of energy by producing NMC batteries is 180$/kWh while the energy density of said battery is at 1/3 of its theoretical energy density. This means that the cost will be $60/kWh if NMC/graphite battery is utilized at its specific energy density. To get an estimation of the cost to produce such energy by using SSFC cells, we have gathered the cost of raw materials from sigma Aldrich, as listed below, to estimate the cost difference between the material of NMC/graphite full cell and SSFC.

Material	NMC	Graphite	Sulfur	Silicon	Lithium
Cost($/g)	15.1	0.50	3.21	0.77	2.1

For an NMC/graphite full cell, every 1g of NMC will need 0.51g of graphite according to the weight balance equation of a full cell battery, with the NPC capacity being 170mAh/g, and the graphite capacity being 330mAh/g:

$$C_{anode}(\frac{mAh}{g}) * m_{anode}(g) = C_{cathode}(\frac{mAh}{g}) * m_{cathode}(g)$$

As such, the overall cost of a NMC/graphite battery will be

$$1\text{g} \times \frac{\$15.1}{\text{g}} + .51\text{g} \times \frac{\$0.5}{\text{g}} = \frac{\$15.35}{(1+.51)g} = \frac{\$10.165}{g}$$

While the weight balance situation of a SSFC is calculated to be 1g of $Li_{22}Si_5$ weight balances with 1.174g of S. 1g of Li_7Si_2 using equation x. Since $Li_{22}Si_5$ consists of 52.1 wt% Li and 47.9 wt% of Si according to its molecular mass, a balanced SSFC will need .521g of Li, .479g of Si, and 1.174g of S. And such the overall cost of a SSFC battery will be

$$.521\text{g} \times \frac{\$2.1}{\text{g}} + .479\text{g} \times \frac{\$.77}{\text{g}} + 1.174\text{g} \times \frac{\$3.21}{\text{g}} = \frac{\$5.232}{(1+1.174)g} = \frac{\$2.41}{g}$$

Thus, according to the calculated overall price, the overall cost ratio of a NMC/graphite full cell to a SSFC is \$10.165/\$2.41 = 4.22:1

With the SSFC having an theoretical energy density of 1968 kWh/kg, which is 3.25 times of the NMC/graphite full cell, the lowest cost needed to produce a SSFC can be

$$\frac{\$180}{\text{kWh}} \times \frac{1}{4.22} \times \frac{1}{3.25} = \$13.12/kWh$$

Rates calculation

The rates for the half-cells are calculated based on the following equation:

$$m_{active\ material} \times C_{theoretical} = I_{1C}$$

Where C is the theoretical capacity of such active material, and the 1C rate is defined as the battery will need 1 hour to charge and discharge if it is at its theoretical capacity.

As such, the rate for sulfur half-cell was calculated to be:

$$5.22mg \times \frac{1675mAh}{g} = 8.75mA = I_{1C}$$

Which also allow us to calculate the rates C/50 and C/10.

$$I_{\frac{C}{50}} = \frac{I_{1C}}{50} = 0.175mA$$

$$I_{\frac{C}{10}} = \frac{I_{1C}}{10} = 0.875mA$$

Using the same method, the rate for silicon half-cell was also calculated:

$$4mg \times \frac{4200mAh}{g} = 16.8mA = I_{1C}$$

$$I_{\frac{C}{50}} = \frac{I_{1C}}{50} = 0.336mA$$

$$I_{\frac{C}{10}} = \frac{I_{1C}}{10} = 1.68mA$$

Since the same electrodes were used for full cell assembly, and the electrodes weren't properly weight balanced, the rate used for full cell cycling was the sulfur half-cell rate due to the sulfur electrode being the limiting factor.

Specific Energy calculation

The specific energy of the battery (E) is calculated based on the total capacity of the battery (Q), nominal voltage window of the battery (V), anode active material weight (m_A) and cathode active material weight (m_c), as shown in the equation below. (Note that although the battery's anode and cathode material are not energy balanced, the actual mass is used for calculation instead of energy balanced weight)

$$E = \frac{Q * V}{m_A + m_C}$$

Using the first cycle as an example, the capacity is 0.4521 mAh. The specific energy is then calculated by:

$$E = \frac{0.4521mAh * 2V}{(5.5mg + 4mg)} = 95.18\ Wh/kg$$

Weight balance calculation

To balance the anode and cathode in a full cell, the total capacity of the electrode should match with each other. To find the correct weight balance ratio of sulfur to silicon loading, the following calculation was carried out:

$$m_{si} \times \frac{4200mAh}{g} = m_s \times \frac{1675mAh}{g}$$

$$\frac{m_s}{m_{si}} = \frac{2.5}{1}$$

Li amount calculation

To decide the amount of lithium used to assemble the cell, the minimum amount of lithium needed by the system was first calculated. To do so, the lithium needed to lithiate the electrodes and the lithium consumed by the SEI during the condition cycles were added to get an estimation.

The Li needed to lithiate the electrodes can be calculated through molar mass, and should be decided by the higher lithium consumption electrode since the anode and cathode weren't weight balanced.

For Sulfur:

$$S \rightarrow Li_2S$$

$$5.22mg\ S \rightarrow 0.171mmol\ S\ \rightarrow 0.171\ mol\ Li_2S \rightarrow 0.343mmol\ Li\ \rightarrow 2.382mg\ Li$$

For Silicon

$$Si \rightarrow Li_7Si_2$$

$$4mg\ Si \rightarrow 0.1424mmol\ Si\ \rightarrow 0.0712\ mol\ Li_{22}Si_5 \rightarrow 0.6266mmol\ Li\ \rightarrow 4.35mg\ Li$$

The SEI Li consumption of the conditioning cycles is estimated base on the Coulombic Efficiency of the half-cells, as shown:

$$m_{li} \times (1 - CE_1) + m_{li} \times (1 - CE_2) + m_{li} \times (1 - CE_3)$$

Where m_{li} is the Li used for that cycle of discharge, Since there is unlimited Li in half-cells, we can estimate m_{li} to be constant and equal to the theoretical Li mass that is calculated previously.

As such, the SEI Li consumption of the sulfur electrode was estimated to be:

$$2.382mg \times [(1 - 0.88) + (1 - 0.88) + (1 - 0.97)] = 0.643mg$$

And the SEI Li consumption of the silicon electrode will be:

$$4.35 \times [(1 - 0.84) + (1 - 0.9) + (1 - 0.92)] = 1.479mg$$

With these calculated, the minimum amount of Li we need to put into the system will be:

$$4.35 + 0.643 + 1.479 = 6.47mg$$

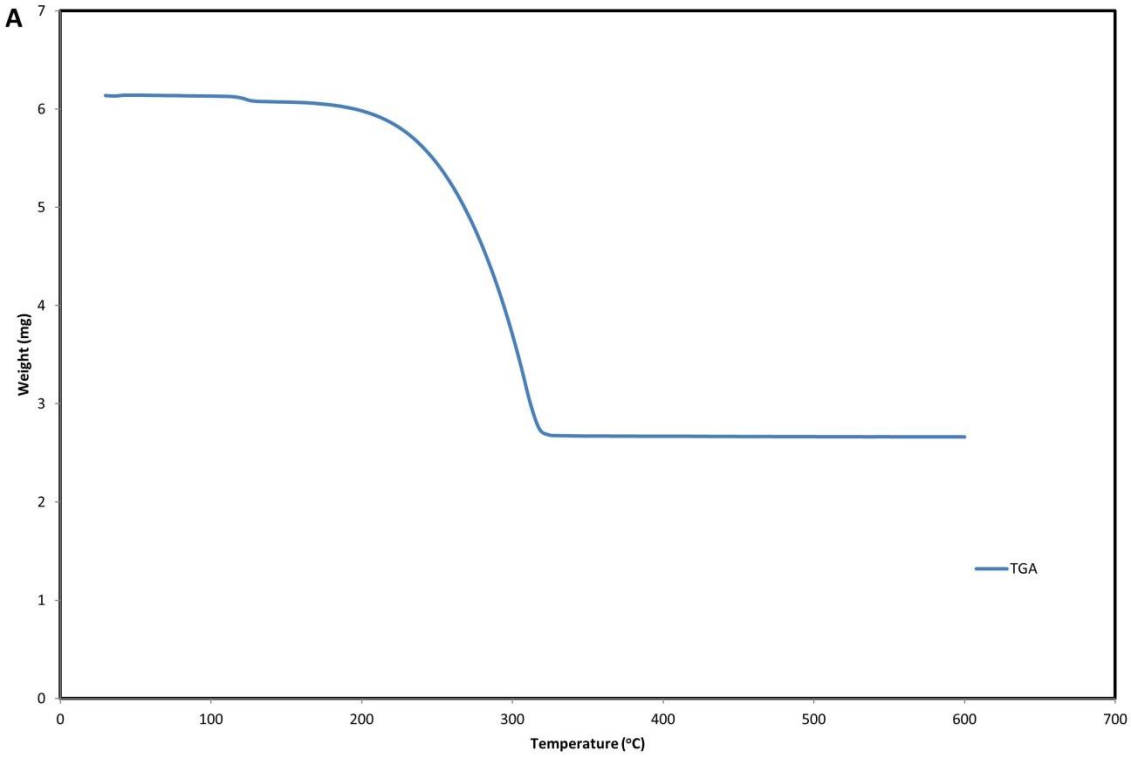

Figure 17: Thermogravimetric analysis of acetylene black sulfur composite.

3.2 Plateau Targeted Conditioning: an Additive-Free Approach Towards Robust SEI Formation in Li-S Batteries for Enhanced Capacity and Cycle Life

(See Next Page)

Plateau Targeted Conditioning: An Additive-Free Approach towards Robust SEI Formation in Li-S Batteries for Enhanced Capacity and Cycle Life

Jeffrey Bell[1,†], Rachel Ye[2,†], Daisy Patino[1], Kazi Ahmed[3], Andrew Scott[1], Leon Peng[4], Zafer Mutlu[1,2], Mihri Ozkan[3,*], and Cengiz S. Ozkan[1,2,*]

†These authors contributed equally to this work.

[1]Materials Science and Engineering Program, University of California Riverside, CA 92521

2Department of Mechanical Engineering, University of California Riverside, CA 92521

3Department of Electrical and Computer Engineering, University of California Riverside, CA 92521

4Department of Computer Science and Engineering, University of California Riverside, CA 92521

Abstract

Lithium-sulfur (Li-S) is one of the most promising next-generation lithium-ion battery systems due to its high theoretical specific capacity. However, Li-S batteries suffer from a short cycling life, poor mechanical stability and low coulombic efficiency. Developing a robust solid electrolyte interphase (SEI) plays a critical role in alleviating these issues. Current approaches for a robust SEI are mostly based on using additives, which negatively impact the energy density. Herein, newly developed electrochemical conditioning techniques were applied to study their effects on the formation of the SEI in Li-S batteries. The dynamic mechanisms in the battery associated with each conditioning technique were investigated using city and highway models based on real world driving conditions. City and highway models incorporated various electrochemical characterization techniques while introducing varying levels of cycling stress. As an additive free approach, the novel plateau targeted conditioning method improves Li-S SEI formation that increases battery capacity and cycling stability. This work will pave the way for the realization of additive free approaches to improving the performance of Li-S batteries.

1. Introduction

With demand for fossil fuels in decline while clean energy becoming more cost efficient, automotive companies are adopting electric vehicles (EV) for future transportation needs. However, current lithium ion battery (LiB) technologies are not capable of the

performance required for EVs to be economically competitive with internal combustion engines. Conventional EV battery packs utilize lithium nickel manganese cobalt oxide (NMC) or lithium nickel cobalt aluminum oxide (NCA) cathodes capable of up to 300 highway miles due to a limited cathode capacity of 170 mAh/g. In order to facilitate further implementation of EVs, battery technologies capable of yielding longer driving ranges at lower prices need to be explored. One of the primary materials under consideration for next generation of LiBs is sulfur. Sulfur is a high capacity, energy dense, and abundant cathode material with a theoretical capacity of 1675 mAh/g and energy density of 2600 Wh/kg. However, lithium-sulfur (Li-S)s' electrochemistry presents several challenges that inhibit it from being commercialized.[1]

Li-S batteries face three major challenges: detrimental volumetric changes, poor electrical conductivity, and polysulfide shuttling.[2] Volumetric changes result from the density difference between sulfur and lithium sulfide[3]. An 80% volume change mechanically expands and contracts the electrode, degrading its structure and conductive network with each cycle. Sulfur's poor electrical conductivity requires a large amount of carbon additive to achieve practical current rates greater than C/10 or 1.675 mAh/g.[4] However, excess additives decrease an electrode's sulfur content and creates deadweight in the electrode. This limits the cell's potential energy density, making it impractical for industry. Polysulfide shuttling in Li-S results from the long chain polysulfides (Li_2S_8 - Li_2S_4) being highly soluble in ether electrolytes, which are commonly used in Li-S batteries due to their preferred high ionic conductivity.[5] Once (Li_2S_8 - Li_2S_4)

dissolves in the ether based electrolyte, polysulfides shuttle from the sulfur electrode across the separator collecting on the counter electrode (lithium foil). These polysulfides form an insulating layer during delithiation, reducing ionic conductivity while causing capacity loss from dead sulfur.[6]

Various methods have been demonstrated to alleviate these aforementioned issues in sulfur's electrochemistry, each having varying degrees of improvement on the cell's performance. For example, to prevent mechanical pummeling in sulfur electrodes, researchers have proposed using the structures engineered with void spaces.[7] The engineered void spaces have extra room to accommodate expansion of sulfur but reduces the overall volumetric energy density of the cell. To tackle the issues of poor electrical conductivity, a combination of carbon nanotubes (CNTs), graphene, reduced graphene oxide (rGO), and other assorted highly conductive carbons in varying amounts have been utilized.[8,9] The conductive carbons help mitigate conductivity issues but at the expense of adding weight to the battery and increasing cost. To suppress polysulfide shuttling, several groups have employed various thin films or core shell structures such as graphene paper and pomegranate like carbon structures.[10] [11] These structures trap polysulfides within the cathode, increasing performance; however, the methods utilized to achieve this are impractical for commercialization. Beyond issues in Li-S material electrochemistry, issues exist in the Li-S battery electrochemistry.

Common issues in Li-S battery electrochemistry resulting from cycling are electrolyte degradation, poor solid electrolyte interphase (SEI) formation, and gas evolution. All of these are common issues found in all LiB systems.[12,13] Among these issues, it is a consensus amongst researchers that SEI formation plays a key role in mitigating the negative behavior of the Li-S electrodes. The most common method for alleviating SEI formation issues is using additives, such as phosphorous pentasulfide, lithium nitrate, polysulfides, and lithium iodide.[14, 15-17] Additive use focusing on robust SEI formation falls under three categories: reduction type, reaction type, and morphology modifier. However, additive use in Li-S tends to have adverse effects on energy density, internal resistance, and cycling stability while additive-free approaches to robust SEI formation have not garnered enough attention.[18, 19]

Herein, we develop an additive free conditioning technique towards robust SEI formation that targets specific voltage plateaus Li-S batteries. Current practice in Li-S batteries is to slowly discharge/charge (C/20 - C/100) for one to three cycles before increasing to higher current rates.[20, 21-24] However, conditioning practices are seldom understood, yet it has the potential to increase cell performance at little cost regardless of electrode design. We present three different methods for conditioning a Li-S cell tested by models inspired by city and highway driving conditions. Performance and health effects of the three conditioning methods on the cells are investigated using galvanostatic intermittent titration technique (GITT), cyclic voltammetry (CV), galvanostatic cycling with potential limitation (GCPL), and potentiostatic electrochemical

impedance spectroscopy (PEIS). All batteries are cycled under the same city and highway models to ensure comparable results. Currents are calculated based on information gathered from EVs driving rates. Below we show a novel additive-free approach to robust SEI formation for enhanced cycling performance characterized via custom testing models.

2. Methods

2.1. Electrode synthesis

The battery used for the EV testing consists of a sulfur electrode countered by a lithium metal anode. The sulfur electrode was made with 20 wt% poly(acrylic acid) (PAA, 1800 g/mol, Sigma-Aldrich), and 80 wt% acetylene black sulfur composite (ABS) that was made by dissolving 200 mg of sulfur (S, 99.998% trace metals basis, Sigma-Aldrich) in 20 ml of dimethyl sulfoxide (DMSO, Fisher Chemical) at 90 C, heated by a heating jacket (Brisk Heat). 129 mg of acetylene black (Alfa Aesar, 50% compressed) was then added to the solution. The solution was stirred for 3 hours before the heating jacket was removed, and the solution was allowed to cool while stirring. The resulting ABS composite was then washed by anhydrous ethanol (Decon Labs, Inc.) several times to ensure the removal of DMSO and dried at 60 C for 24 hours. To make the sulfur electrode, 20 wt% PAA (450,000 MW) and 80wt% ABS was mixed with 1-methyl-2-pyrrolidinone (NMP, Sigma-Aldrich) and then casted on a large piece of aluminum foil

(Alfa Aesar, 0.025 mm thickness, 99.45% purity) by a doctor blade (MTI Automatic Thick Film Coater, BYK Doctor Blade). The casted electrode sheet was then dried in a convection oven (Cole-Parmer, Stable Temp) at 60 C for 24 hours. The electrodes were calendered with 0.04 mm gap using a calendering machine (IRM) before being constructed into a coin cell.

2.2. Electrochemical characterization

To make the sulfur half cell, a lithium foil electrode (16 mm in diameter) was first put inside a negative cap (MTI type 2032 coin cell case). Next, separators (Celgard 25 µm 3501) of various sizes were placed on top to prevent any possibility of shorting. Sulfur electrode (16 mm in diameter) was then placed on top followed by two spacers, a spring, and the positive cap while electrolyte was added in between (1:1 DOL:DME, 1wt% $LiNO_3$, 1M LiTFSI). The battery was then sealed using a battery crimper (MTI, MSK-160D). All cell assembly was done inside an Ar filled glovebox (H_2O < 0.5 ppm, O_2 < 0.2 ppm, Vacuum Atmosphere Co.). The battery was then tested under room temperature with a Bio Logic (BCS 810 Testing Module) using different testing methods, including GCPL, CV, PEIS and GITT in voltage window ranging from 1.7 V to 2.8 V.

3. Results and discussion

Various battery testing methods were used to evaluate cells pre/during/post simulated driving. The sulfur electrodes were made using an ABS composite with PAA as detailed in the methods section. The Li-S cells were then assembled into coin cells with lithium foil acting as the counter electrode. The sulfur loading for each battery is 2.5 mg/cm^2. The cells were then conditioned using three different methods: Method 1 applies a current rate of C/50 (0.175 mA) during discharge and charge for 3 cycles. This is the common average of conditioning methods reported by researchers and thus it was used as the datum in this study. Method 2 applies current pulses at 10 minute intervals at C/50 for 3 cycles. The rest between current pulses allows for voltage equalization, which will prolong the discharge process and maximize material reduction in the electrode. Lastly, Method 3 applies a rate of C/50 during discharge from 2.8 V to 2.1 V and a rate of C/100 (0.0875 mA) from 2.1 V to 1.7 V. This method avoids excess polysulfide shuttling in the voltage plateau associated with the formation of long chain polysulfides, while targeting the lower voltage plateau, at a slower rate, associated solid formation on the carbon matrix, 2.1 V. All methods charge batteries at a rate of C/50; each conditioning procedure is repeated for three cycles. Fig. 21c-f, the proposed schematic for datum and plateau targeted conditionings effect on SEI formation along with the resulting effects on the battery system. A unconditioned control battery was tested in conjunction. The performance results of the unconditioned batteries can be found in the supplementary information (Fig. S3).

The cells then underwent two different testing models, one based on real world driving conditions found in the city (city model) and the other based on real world driving conditions found on the highway (highway model). Each model simulates a driving distance of 36.5 miles, the average distance driven by a person each day. At the end of each simulated day cells were fully charged, simulating users charging EVs overnight, and PEIS was taken. This driving/charging cycle was repeated 7 times (week) before a cycle of GITT. GITT was used to examine lithium diffusivity within the cell, giving a detailed picture of changes to the electrodes conductive network. Ten full discharge/charge cycles were then applied to the cell to simulate aging. Post aging, CV was instituted to check the health of electrochemical reactions. Lastly, the driving-charging-PEIS-GITT-aging-CV process was repeated four times while doing PEIS at points of interest.

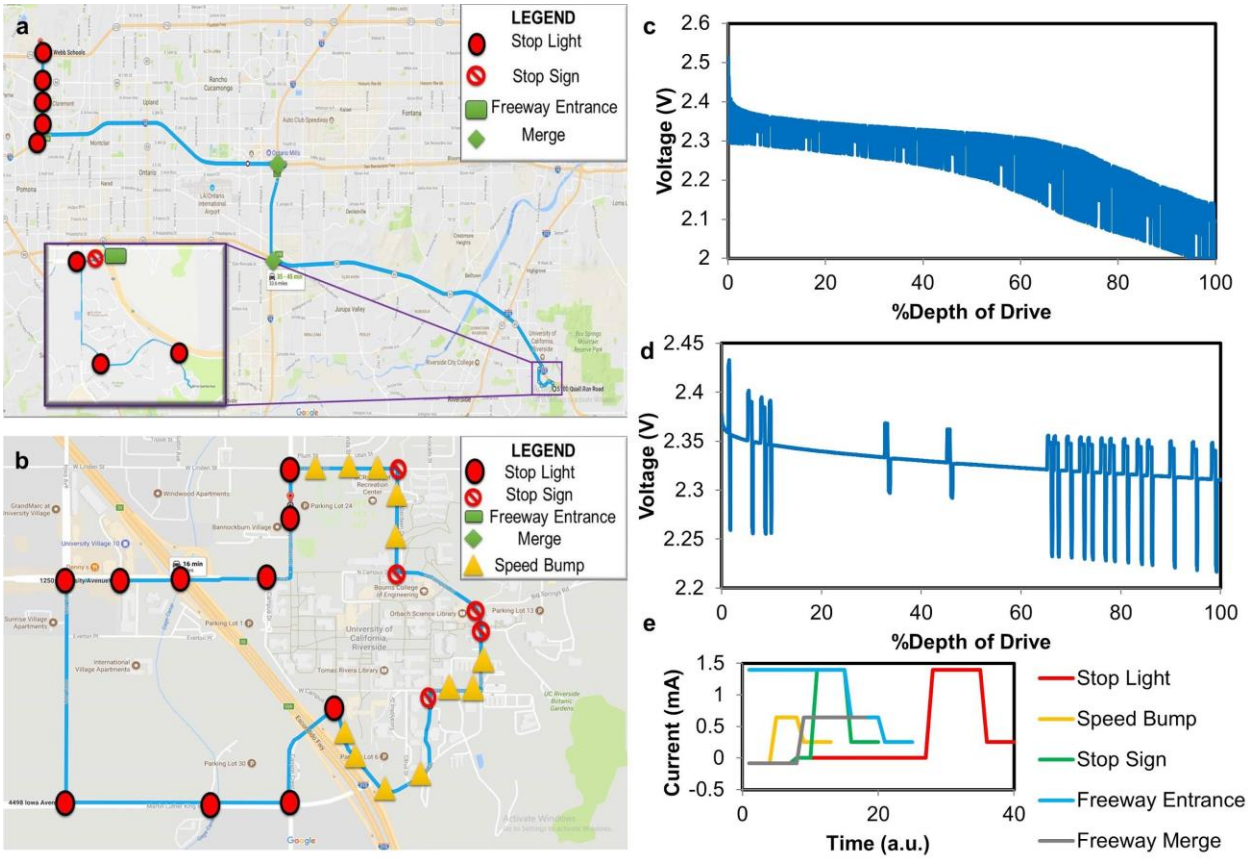

Fig 18. (a) Map of city driving route from google maps. (b) Map of highway driving route from google maps. (c) Voltage variation of Method 1 battery going through city cycling model (Riverside/Claremont, CA). (d) Voltage variation of Method 1 battery going through highway cycling model. (e) Current change of each simulated condition used in city and highway model.

The city model was designed to simulate different discharge/charge rates a EV battery was subjected to while driving in a city. Contrary to conventional constant current rated cycling used in research, the city model consists of a series of different discharge/charge rates reflecting different energy consumption needs in a EV. To simulate real world

driving conditions, corresponding discharge/charge rates were estimated based on data released for the Tesla Model S. From Tesla's official website, the discharge rate of the 75D Model S is around C/5 at 60 mph.[25] Considering that the specific capacity of a Li-S cell is 6 times the specific capacity of current commercial cells, the base discharge rate used for the city and highway models was calculated as C/30. Based on the constant driving condition, light and hard acceleration were simulated using C/10 and C/5; C/100 was used to simulate energy recovery during braking. A driving route was designed based on Google maps, shown in Fig. 18a, consisting of lights, stop signs, turns, freeway mergers, freeway entrances/exits and speed bumps. Fig. 18e shows the detailed rate changes of the city model. In a similar fashion, a highway model was designed, Fig. 18b. Comparatively, the highway model contains less current rate variation resulting in a reduced stress load for batteries tested on the highway model. As a result, city and highway cycled batteries give different performance characteristics. Current rates associated with different speeds can be found in table 3, while common driving variable test protocols can be found in table 2.

Fig. 18c and 18d, voltage fluctuations of city and highway models, respectively, during a simulated driving day. According to Fig. 18c, a fully charged battery experiencing severe current fluctuation from the city model will discharge to around 2 V. Crossing the 2.1 V threshold indicates that the battery has passed the higher kinetic region (Li_2S_8-Li_2S_3) entering the lower kinetic region (Li_2S_2-Li_2S).[26] Fig. 18d, batteries experiencing reduced current fluctuation from the highway model will remain in the higher kinetic region

(Li_2S_8-Li_2S_3). The difference in end voltages is an indicator of stresses placed on the battery, although both simulate the same driving distance. Batteries cycled by the city model experienced increased stresses than those cycled by the highway model.

Table 2. Current rate used to simulate driving interactions

City & Highway Model		
Driving Interaction	**Condition**	**Current**
Stop Sign	Brake, Stop, Hard Acceleration, Constant Driving	C/100, 0, C/5, C/30
Speed Bump	Brake, Light Acceleration, Constant Driving	C/100, C/10, C/30
Stop Light	Brake, Rest, Hard Acceleration, Constant Driving	C/100, 0, C/5, C/30
Freeway Entrance	Hard Acceleration, Light Acceleration, Constant Driving	C/5, C/10, C/30
Freeway Merge	Brake, Light Acceleration, Constant Driving	C/100, C/10, C/30

PEIS is a non-destructive method that characterizes the integrity of the electrode-electrolyte interface, passivation layers, electronic conductivity of electrode material, diffusion of lithium within electrode, and diffusion of lithium-ions in electrolyte near electrode surface.[27] Complex impedance was measured for a selected number of frequency points between the bounds of 10 kHz and 10 mHz. Fig. 20e shows the electrical equivalent circuit used to model the impedance of Li-S cells at a fully charged state. Additionally, raw experimental data along with the curve fitted experimental data is depicted in Fig. 19e and 19f. All batteries for each testing model were investigated with PEIS post day of driving and post GITT, aging, and CV (non-driving EIS data are available in the supplementary document, Fig. S4 and S5).

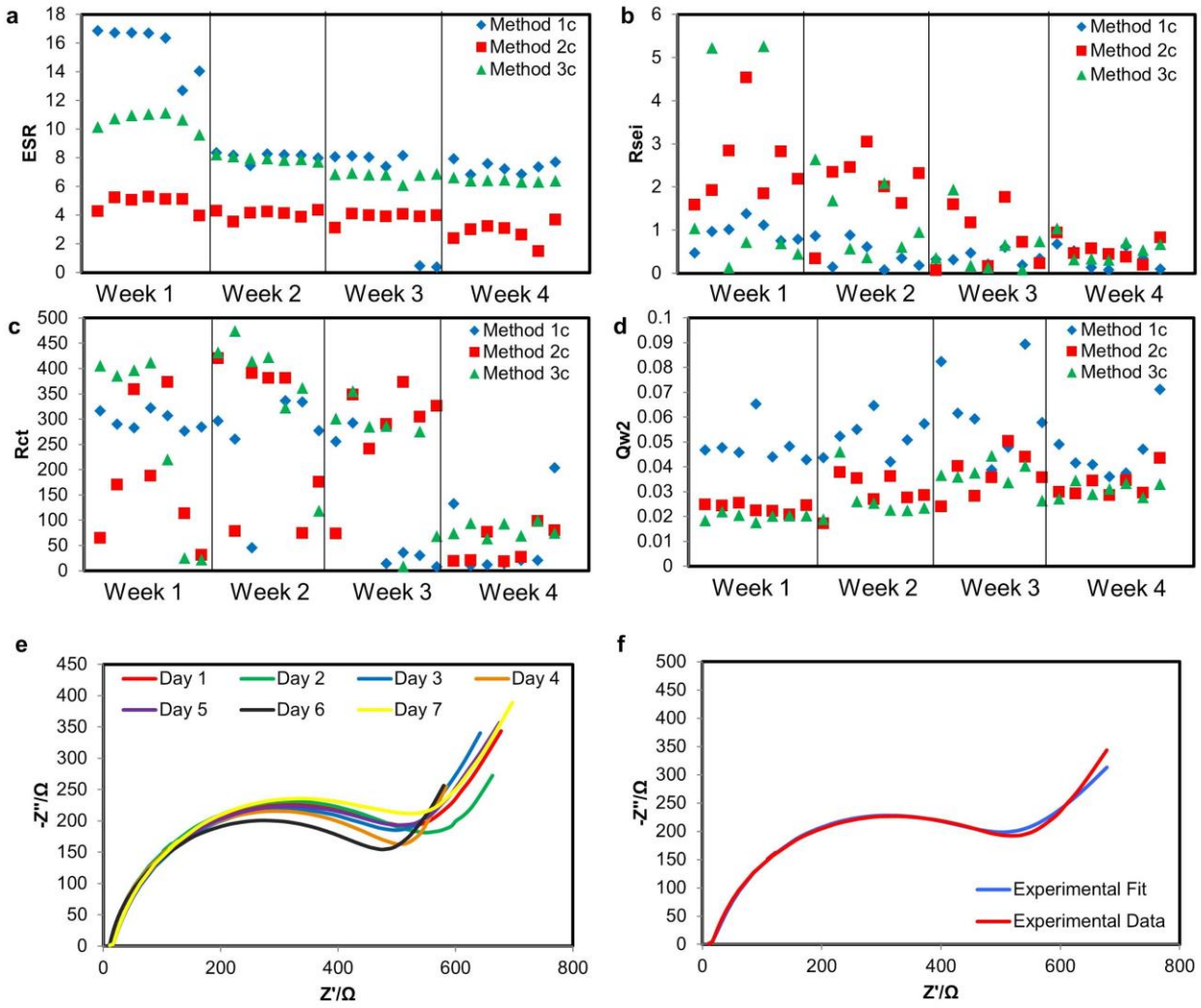

Fig. 19. Impedance parameters of batteries tested by the city model after each driving days (a) ESR. (b) Rsei. (c) Rct. (d) Qw2. (e) Experimental PEIS curves for simulated week 1 of driving for Method 3. (f) Experimental data vs curve fitted data

Value of the equivalent series resistance (ESR) represents the total resistance contributed by solution resistance, charge transfer resistance, and contact resistance in the batteries.[27] Fig. 19a shows the evolution of ESR for the city model. City ESR is highest

for Method 1 battery and lowest for Method 2 battery. High ESR resistance for Method 1 battery can be attributed to the corrosion of the lithium metal anode. This results from poor solid-electrolyte interphase (SEI) formation exhibited in Fig. 19b by the low Rsei values. A previous study showed that once polysulfide concentration in the electrolyte passes a threshold ($c > 0.5$ M), polysulfides corrode the lithium metal, breakdown lithium SEI, form dendrites, and creates dead lithium[28]. This ultimately creates excess resistance in the lithium anode increasing ESR (Fig. 19a). Contrarily, city ESR for Methods 2 and 3 batteries provide evidence of electrochemical durability, indicated by the stability in ESR from week 1 to 4. Electrochemical durability in a half cell is important but hard to achieve due to the presence of a lithium counter electrode, shown by Delpuech at el.[29] Method 1 battery shows a ESR drop from week 1, this concurs with drop in the Rct and an increase in Qw2 from week 1 to week 2 where Qw2 represents lithium capacitance in the electrolyte. Low ESR values for method 2 battery are attributed to changes in electrolyte ionic conductivity. Unlike method 1 battery, where it is believed the polysulfide electrolyte concentration passed a threshold, method 2 battery stayed in the beneficial range of polysulfide shuttling ($0.1 \text{ M} < c < 0.5$ M). This prevents lithium corrosion while also enhancing ionic conductivity.[30] Therefore, method 2 battery which has more polysulfide shuttling, based of capacity differences, has the lowest ESR.[27] This difference in polysulfide shuttling is determined by SEI layer quality. Comparing to Method 2, Method 3's plateau targeted constant current rate allows formation of a robust SEI layer with minimal defects which greatly mitigates

polysulfide shuttling. A secondary benefit of polysulfide mitigation is reducing parasitic effects on the lithium anode. Parasitic reactions cause the formation of an unstable SEI layer on the lithium anode, while stable SEI attributes greatly to the stability of the battery. A robust SEI layer forming on both electrodes is supported by the stability in coulombic efficiency. The schematic for this proposed mechanisms is depicted in Fig. 21e and 21f.

Fig. 19a shows Rsei changes for the city model. Rsei quantizes the resistance associated with the formation of the SEI layer, a higher Rsei indicates thicker SEI layers. Sulfur does not natively form any permanent passivation film similar to SEI layers observed in silicon or carbon electrodes.[31] We propose the SEI resistance observed in our sulfur electrodes mainly originate from the carbon additive, but may also be affected by polysulfides and electrolyte composition. Shown in Fig. 19a, it is observed that Method 2 battery has the highest resistance value compared to Methods 1 and 3 batteries. Method 2 battery's high Rsei results from the distinct characteristics of this conditioning method that utilized pulsed currents. We propose that the pulsed currents during the conditioning cycles cause volumetric expansion of sulfur to rupture the SEI layer prematurely formed during rest periods.[32] Each consecutive pulse repeats this detrimental process, causing an thick, nonhomogeneous SEI layer to form on the cathode, which results in inefficient lithium-ion conducting pathways.

The change in Rct for the city cycling is shown in Fig. 19c. Rct is the charge transfer resistance at the electrode electrolyte interface which gives insights into the kinetics of the battery.[27] As shown in Fig. 19c, all cells show a stabilizing trend in their kinetics during week 4. For weeks 1 to 3, all cells exhibit erratic behavior resulting from electrode degradation, mechanical or chemical, due to continued stresses placed on the cell by the city cycling model.

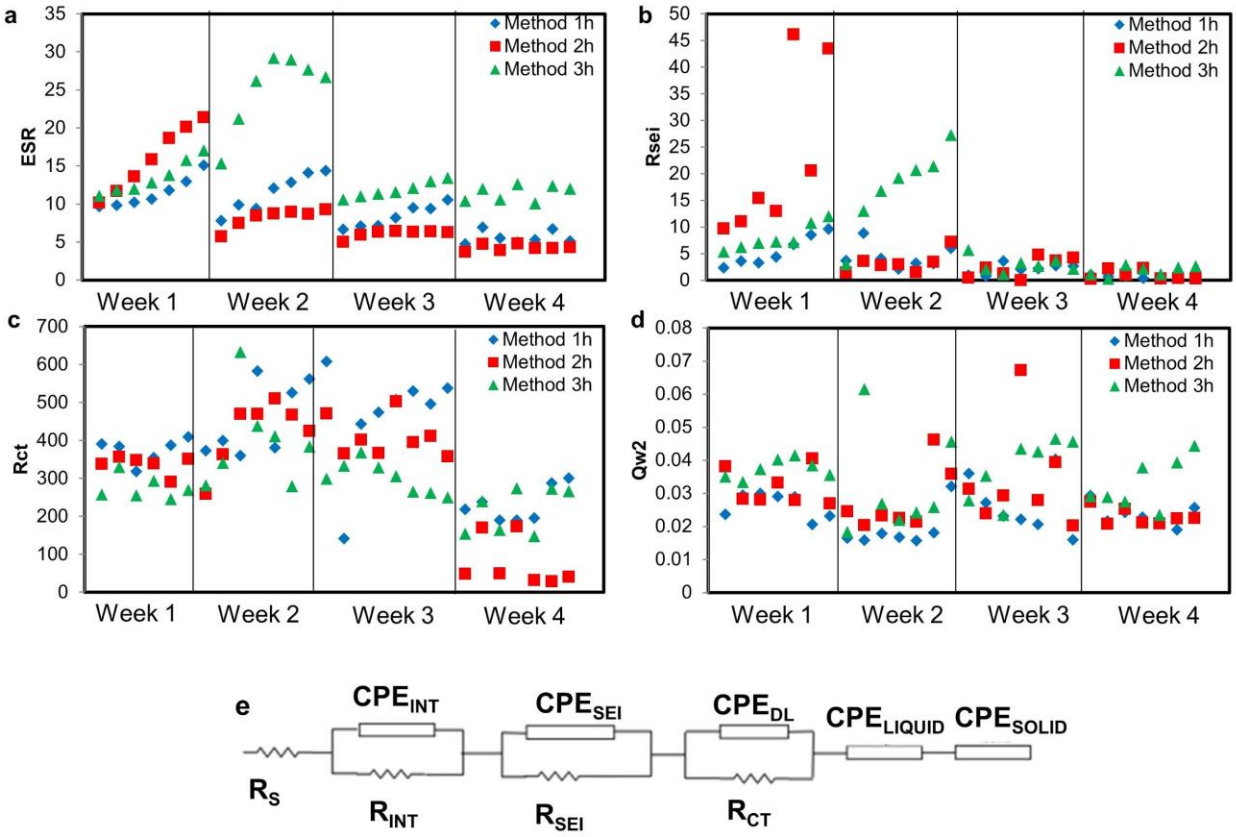

Fig. 20. Impedance parameters of batteries tested by the highway model after each driving days (a) ESR. (b) Rsei. (c) Rct. (d) Qw2. (e) Electrical equivalent circuit used for PEIS.

The evolution of the ESR and Rsei for highway cycles is shown in Fig. 20. ESR increases for all batteries week 1, but stabilizes by week 3. In contrast to Methods 1 and 2 batteries, ESR for Method 3 battery continue to increase during week 2. ESR is dominated by solution resistance, or electrolyte conductivity, but also takes into account changes in SEI resistance. This relationship is shown Fig. 20b which the increase in ESR is attributed to the spike in Rsei week 2.

Rsei for all batteries increases during week 1 but stabilize by week 2 with the exception of Method 3 battery. In city cycling, it is observed that the SEI originates from the carbon additive but may also incorporate polysulfides into the measurement. For highway cycling, we propose that the structure of the delithiated polysulfides also affects the Rsei. The highway cycling model's discharge never reaches the second plateau (2.1 V), as shown in Fig. 18d, indicating the sole formation of electrolyte soluble long chain polysulfides. When long chain polysulfides delithiate into sulfur, the resulting sulfur particles gather on the conductive network and SEI layer. Sulfur gathering on the SEI layer can be mistaken as a contributing factor to Rsei. As sulfur becomes increasingly densified on the SEI layer with each successive cycle, Rsei increases proportionally, shown in Fig. 20b. This phenomenon occurs in all batteries during week 1 but only exists for Method 3 battery in week 2. The increasing Rsei for Method 3 battery during week 2 results from it having a stronger SEI layer, mitigating polysulfide shuttling. It is speculated that the other two methods allow more sulfur loss located on the surface layers of the electrode to polysulfide shuttling, while Method 3 retained the majority of surface layer sulfur longer. Once the surface layer of sulfur is lost to polysulfide shuttling, Rsei stops increasing.

The change in Rct for the highway model is shown in Fig. 20c. Week 1 to week 4 show a stabilizing trend for all batteries. Unlike the erratic behavior evidenced by Rct city cycling in Fig. 19c, highway cycling does not experience this erratic behavior. We propose that the difference stems from the varying stresses placed on the batteries.

Shown in Fig. 18a and 18b, highway cycling only experiences 65 current rate changes for total drive, compared to 270 current rate changes in city cycling. Hence the current rate changes in highway cycling do not cause sufficient stress to damage the electrode-electrolyte interface. As such, batteries subjected to all methods show stabilizing trends, with Method 3 battery experiencing the least resistance. Method 3 battery's low resistance results from a better electrode-electrolyte interface built during the conditioning cycles.

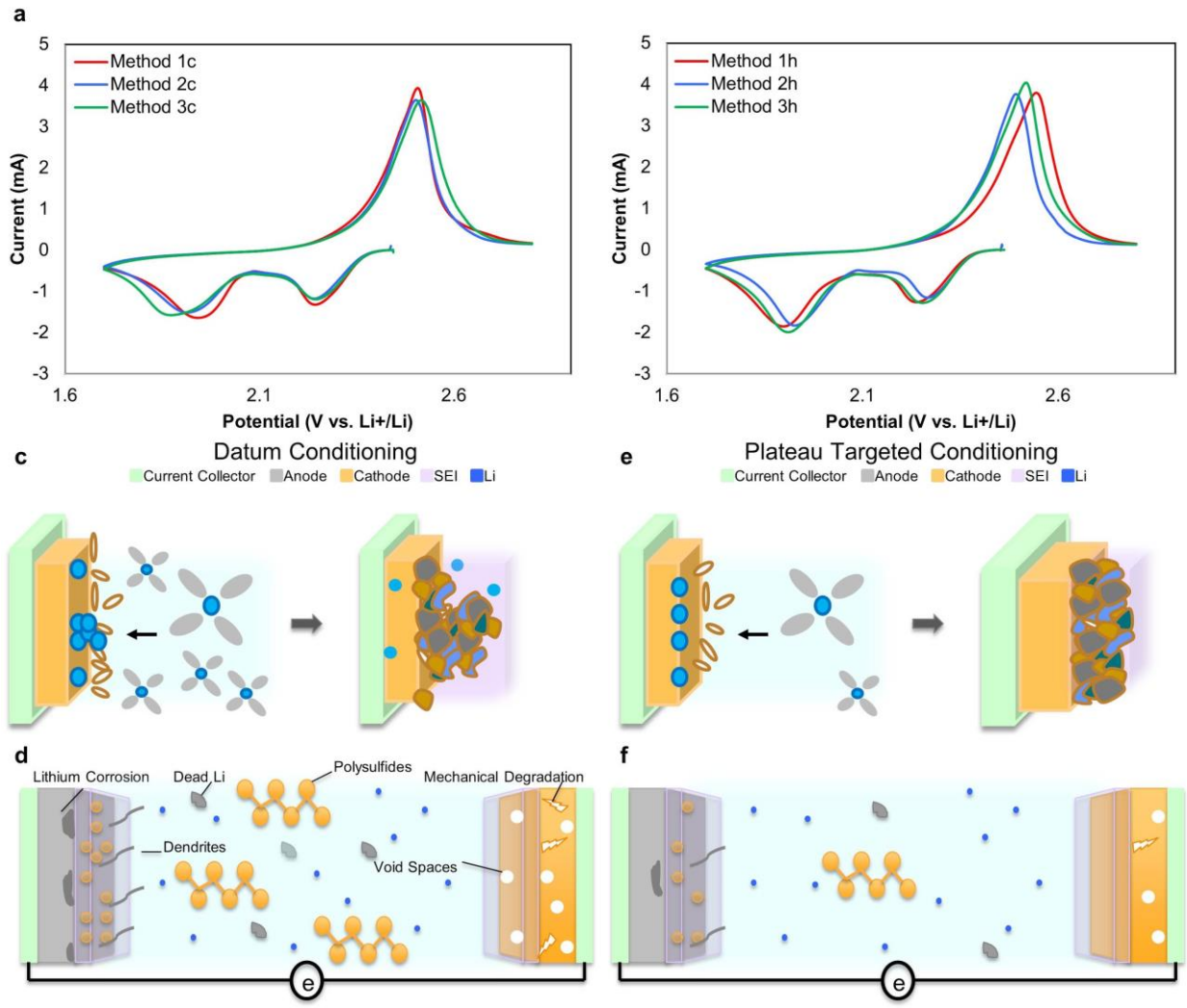

Fig. 21. (a) CV of Method 1, 2, & 3 batteries tested by city model. (b) CV of Method 1, 2, & 3 batteries tested by highway model. (c) Proposed SEI formation for datum conditioning. (d) Proposed resulting effect of datum conditioning. (e) Proposed SEI formation for plateau targeted conditioning. (f) Proposed resulting effect of plateau targeted conditioning.

CV is a electrochemistry technique that measures current generated by the battery while cycling the battery potential at a given rate. When an electrode is cycled under CV, the reduction of electrode material causes current to increase forming a cathodic peak. When the surface material has been reduced, lithium ions diffuse through the surface layer to continue the reduction process, thus causing the peak current to drop. As an adaption to the previous theory, a battery that has better kinetics will be able to reduce surface material faster, thus causing the cathodic peak to shift upward in potential. A battery that has greater quantity of active material to reduce will cause a greater peak intensity.[33]

CV for all batteries were carried out in a voltage window of 1.7 V and 2.8 V at each week end. Fig. 21a and 4b show the CV profiles for batteries at week 4 end. The CV curves presented align with typical sulfur CV curves found in literature.[34] Sulfur's CV consists of two cathodic peaks at 2.1 V and 2.35 V, and one anodic peak at 2.35 V. The cathodic peak at 2.35 V corresponds to the formation of long chain polysulfides, while the peak at 2.1 V results from the formation of Li_2S. Slight variations in peak voltage between batteries results from different conditioning methods altering kinetics of the system. Variations in peak voltage is seen in both city and highway model batteries. Fig. 21a, all city model batteries have the same anodic peak voltage of 2.25 V representing long chain polysulfide formation, while peaks representing Li_2S formation varies. Method 1 battery for the city model has the highest Li_2S peak voltage at 1.95 V, Method 2 and 3 batteries have a peak voltage of 1.9 V and 1.85 V respectively. Variance in peak voltage

corresponding to Li_2S results from changes in ionic conductivity due to the differing concentration of polysulfides in the electrolyte.[30] As discussed in the previous section, Method 3 battery is proposed to shuttle a reduced amount of polysulfides comparatively, resulting in the lowest peak voltage. In comparison, Method 1 with the highest quantity of polysulfides, results in the highest peak voltage. Method 1 and 3 batteries also have higher peak intensities than Method 2, indicating higher material reduction, this is further proven in Fig. 7a.

Fig. 21b shows the CV curves for the highway model batteries. Fig. 21a and 21b, Method 1 battery for the highway model have lower cathodic and higher anodic peak voltages compared to Method 1 battery for the city model and the other two highway model batteries. The difference in peak voltages results from reduced cycling stress, minimizing polysulfide shuttling and mechanical degradation. The ionic conductivity boost, resulting from polysulfide shuttling in highway Method 1 battery does not compensate for the low ionic and electric conductivity resulting from poor SEI and conductive network. Method 2 and 3 batteries however, have well developed SEI and good mechanical stability. This result in Method 2 and 3 batteries having higher cathodic peak voltages and lower anodic peak voltages than Method 1 battery while having the same order (Method 2 battery peak voltage higher than Method 3 battery peak voltage) with city cycling CV following the same logic. Lastly, the peak intensity of Method 3 battery is the highest, followed by Method 1 and then Method 2 batteries, this is also in accordance with the trend shown in Fig. 7b.

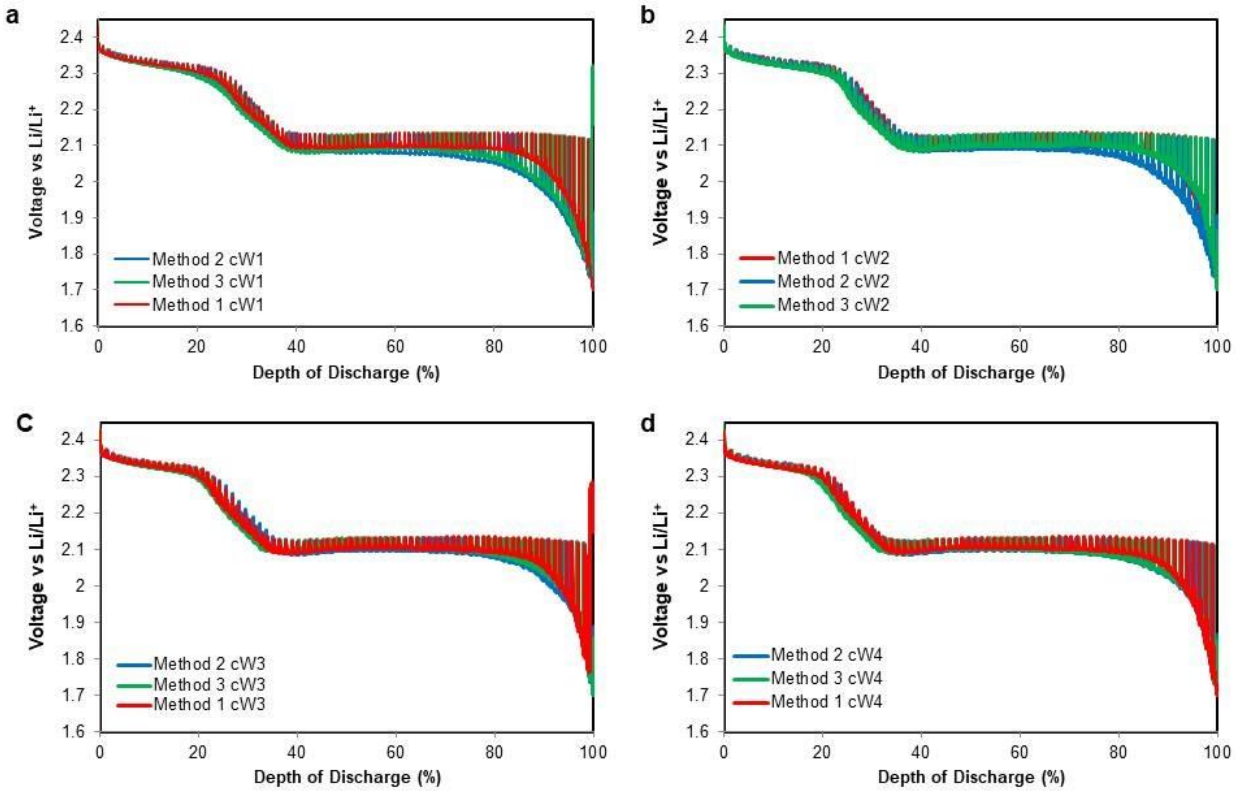

Fig. 22. GITT for Methods 1,2, & 3 batteries after (a) week 1, (b) week 2, (c) week 3 and (d) week 4 of city model driving.

The driving models employed GITT once a week to measure the rate of lithium-ion diffusivity in the electrodes (Fig. 22). GITT uses a series of current pulses, each followed by a relaxation period. Herein, electrodes were pulsed at C/50 for 10 minutes, immediately followed by 10 minutes rests. This interval was repeated until complete discharge/charge. Oscillations in the voltage profile represent changes between the pulsed voltages and steady state voltages.[35] Shorter oscillations throughout the voltage

profile are ideal, indicating minimal voltage excitations during the relaxation period; this represents a homogenous material reduction and improved lithium diffusivity. However, small oscillations may also be indicative of poor material access to the conductive network, referred to as material participation below.[36]

Fig. 22a shows conditioning Method 1 yields the highest rate of lithium diffusivity amongst Methods 2 and 3 after 1 week of the city model. The high diffusivity rate is representative of a network with ease of Li ion transport, high ionic conductivity, and uniform material reduction. Ease of Li ion transport stems from a high concentration of polysulfide shuttling during the conditioning cycles. Consequently, vacancies are created in the electrode from polysulfide shuttling, decreasing material participation and creating better Li ion transport pathways. Additionally, shuttling increases polysulfide concentration in the electrolyte, producing a higher electrolyte ionic conductivity. Ultimately, these factors combined result in uniform material utilization. As a result, excitation of steady state voltage is minimized, and observed as shorter voltage oscillations in Fig. 22a. The Method 1 battery has the smallest voltage oscillations in week 1 and remains as such due to poor material participation.

In contrast, Method 2 battery has the largest voltage oscillations, indicating slower overall rate of material reduction. We infer the overall slower material reduction is attributed to reduced polysulfide shuttling in addition to a larger active material to conductive network ratio. This large ratio results from the current pulses forcing

additional active material to participate in the discharge reaction, furthering mechanical degradation. The low lithium diffusivity also results from the large SEI resistance (Fig. 19b). A large SEI resistance decreases the overall diffusion rate of lithium-ions into the electrode, resulting in Method 2 battery as the least diffusing one. Method 3 battery's improved diffusivity relative to Method 2 battery results from an effective conductive network and low SEI resistance. Method 3 battery's poor diffusivity relative to Method 1 battery however, is due to reduced polysulfide shuttling and increased sulfur utilization.

Ideally, ionic diffusivity in Li-S batteries should remain consistent throughout cycling. Consistency in diffusivity indicates steady active material utilization, minimal polysulfide shuttling, and electrode mechanical stability. However, in Fig. 22b-d, voltage oscillations in each successive week decrease in width, indicating improved lithium diffusivity throughout the city model. The continuing changes in diffusivity results from active material loss, mechanical changes in the electrodes, decreased material participation, or changes in electrolyte polysulfide concentration. It is observed that the voltage oscillations for each battery in Week 4 of the city model are similar, resulting from the increase in ionic conductivity due to polysulfide shuttling. Once electrode degradation reaches the limit, all batteries reach similar conductivities and capacities (Fig. 7). Differences in performance at the end of deep cycling is then determined by factors such as active material participation, SEI quality, mechanical stability, and conductive

network quality in the electrodes. Ultimately, active material participation is the predominant variable contributing to ionic diffusivity at week 4 end in the city model.

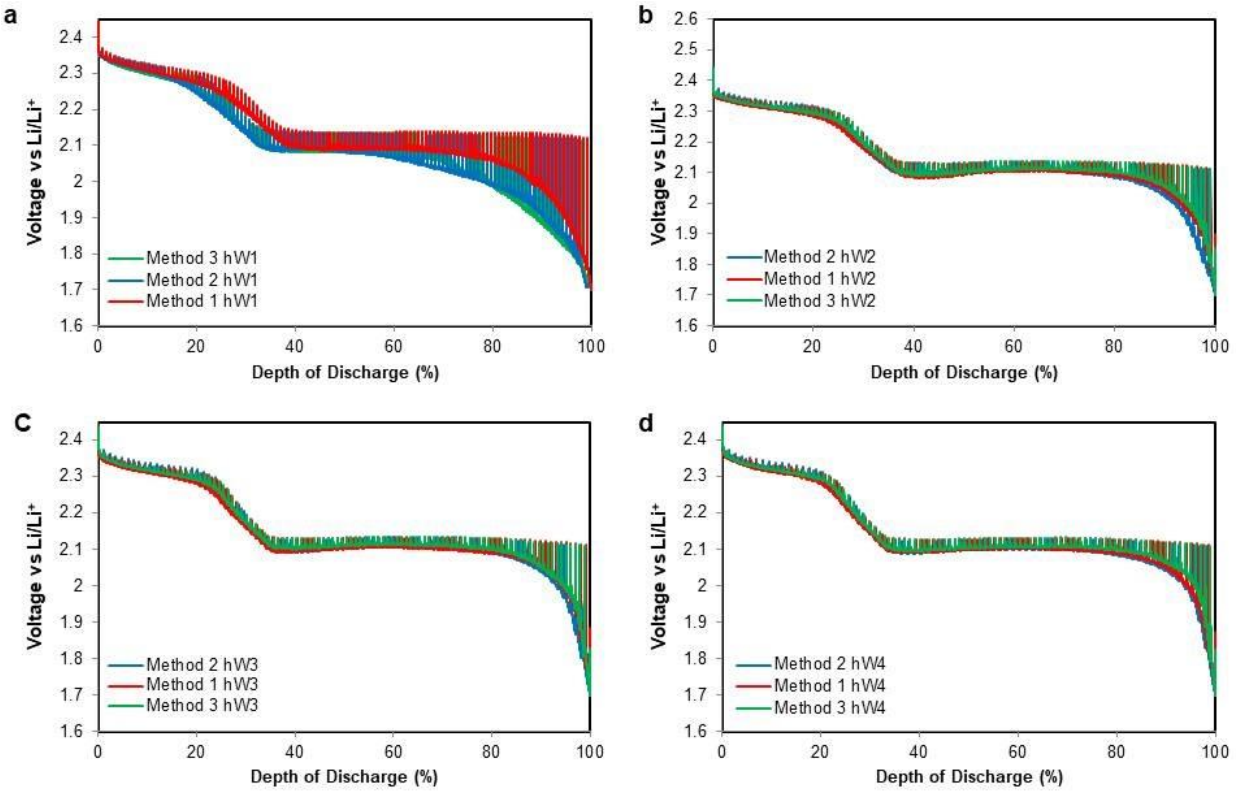

Fig. 23: GITT for Methods 1,2, & 3 batteries after (a) week 1, (b) week 2, (c) week 3 and (d) week 4 of highway model driving.

GITT analysis of the highway model batteries differ starkly to the city model batteries. However, the trend is in accordance with the first two weeks of city model batteries. Highway model GITT profiles appears thinner than the city model profiles. This is due to the minimal amount of volume expansion created by less stressful highway model. As shown in Fig. 18d, the batteries undergoing the highway model stayed in the first

voltage plateau, indicating the sole formation of long chain polysulfides. Long chain polysulfides create up to 20% volumetric change compared to the 80% change in lithium sulfides formed during the second voltage plateau.[3] The small volume change causes the electrode to undergo minimal mechanical degradation resulting in a better conductive network compared to the city model. Another explanation for the shorter voltage oscillations is stated in the PEIS section. As long chain polysulfides delithiate, delithiated polysulfides fall out of electrolyte and disperse evenly on the electrode's conductive network. As a result, the dispersed sulfur is homogeneously attached to the conductive network improving the electrical conductivity of the electrode. As such, method 2 battery does not experience much expansion, and is no longer the least diffusing. The diffusivity of the batteries after week 2 are in the order of polysulfide retention. Method 3 battery has the least polysulfide shuttling while having the worst diffusivity. This is caused by a low concentration of polysulfides in the electrolyte. However, at the end of week 3 and 4, method 3 battery's diffusivity increases and surpasses the other two batteries. This is because all batteries experience polysulfide saturation in the electrolyte over time and reach similar ionic conductivity, but method 3 battery's minimized mechanical degradation due to a robust SEI layer maintained the best electrical conductivity network. Contrary to city model, the conductive network is the predominant variable contributing to ionic diffusivity at week 4 in the highway model; low coulombic efficiency degradation for the highway model further supports this conclusion (Fig. 24d).

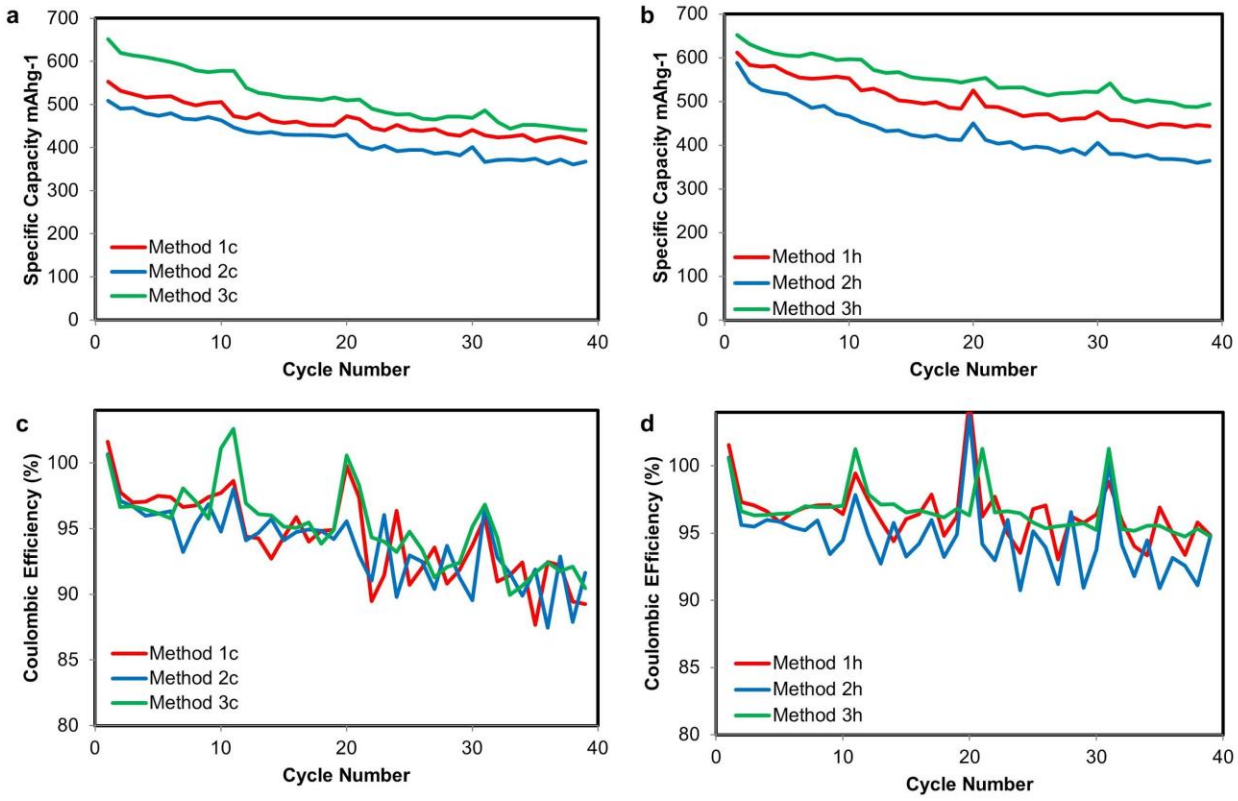

Fig. 24. Galvanostatic cycling with limited potential for Method 1,2, & 3 batteries tested by city model (a) and highway model (b). Coulombic efficiency for Method 1, 2, & 3 batteries tested by city model (c) and highway model (d).

All batteries were discharged/charged for ten cycles post GITT to simulate aging. The corresponding specific capacity vs cycle number for each battery is shown in Fig. 24a and 7b, respectively, for city and highway models. Wave like variation in capacity is caused by changes in room temperature during testing. All batteries show fluctuations in capacity due to temperature changes, it is observed that batteries undergoing condition method 3 fluctuate the least. This results from the stable and high quality SEI

layer created during conditioning.[37] In both the city and highway model batteries, method 3 yields the highest capacity while method 2 yields the lowest. Since all batteries have the same sulfur loading, a higher capacity is indicative of less active material loss during the previous testing routine and more material utilization during aging cycles. Active material loss can be a result of poor SEI layer causing polysulfide shuttling into the electrolyte and the counter electrode, or sulfur detaching from the conductive network during volume expansion/contraction.[27] Better material utilization can result from a better mechanical structure and SEI layer. The reliability of method 3 is observed by the similar starting capacity at city and highway aging cycle 1, city: 651 mAh/g, highway: 652 mAh/g. This aging cycle takes place after all batteries have been driven for 1 week followed by GITT. Method 1 and method 2 batteries however, show noticeable differences in the city and highway model capacities (City: 553 mAh/g and 509 mAh/g, highway: 612 mAh/g and 588 mAh/g). due to the more aggressive stresses of the city model. This indicates that method 3 yields superior capacity retention under stressed conditions.

Method 3 yields higher capacity batteries due to better SEI layer, which decreases further polysulfide shuttling. A robust SEI layer formed during conditioning prevents cracking of the SEI layer during high stress. This reduces material exposure to the electrolyte and prevents the generation of new and excess SEI. Furthermore, the robust SEI layer creates better mechanical stability and ionic pathways, which further stabilizes battery performance, resulting in 440 mAh/g city capacity and 494 mAh/g highway

capacity after 4 weeks of testing. Method 2 yields the lowest capacities, 367 mAh/g for city and 364 mAh/g for highway at week 4, resulting from its increased volumetric expansion relative to the other methods. Volume expansion degrades lithium diffusivity and rate capability of the battery. This is observed in Fig. 22, where Method 2 battery yields larger voltage oscillation under the same current. GCPL capacity is measured by the amount of current battery can take at a specified unit of time before it reaches a set voltage, a large voltage fluctuation will result in a lower capacity. In conjunction with increased volumetric expansion, current pulses create excess SEI. Excess SEI consumes additional lithium salt, carbon additive, and lithium ions which can be attributed to the decreased capacity of Method 2 batteries. Method 1 batteries yields 411 mAh/g city capacity and 444 mAh/g highway capacity at week 4 end. This is due to a weaker SEI than Method 3 and less mechanical degradation than Method 2.

Due to the city model's increased stress relative to the highway model, rate of capacity degradation differs. Fig. 24a shows the city model battery capacities converging toward an equilibrium point, 16.6% difference between method 2 and 3 batteries at the end, while Fig. 24b shows the highway model battery capacities decreasing with similar rates, 26.3% difference between method 2 and 3 batteries at the end. The capacity convergence of the city model batteries is noticeable within the 40 aging cycles because of the high testing stress causing the battery to lose sulfur rapidly to polysulfide shuttling and mechanical degradation. Once the electrolyte reaches polysulfide

saturation, the rate of capacity degradation slows down. As a result, all batteries will reach a similar final capacity, creating a converging capacity plot.

Fig. 24c and 7d show the aging cycle coulombic efficiency (CE) for both city and highway models. Large spikes in CE up to 103% exist at the start of each aging cycle (1st, 11st, 21st, and the 31st cycle) due to GITT testing before aging cycles. GITT disrupts the CE of the following cycle by overcharging the battery and activating sulfur that does not participate normally due to limitations in the conductive network. As a result, the following cycle has an increased discharge capacity and a CE over 100 %. In both Fig. 24c and 7d, method 3 batteries have the highest and most stable CE. A stable CE indicates minimized polysulfide shuttling, consistent conductive pathways, and stability under temperature fluctuations.[38] These advantages results from a robust SEI layer. We propose the robust SEI layer of Method 3 batteries traps polysulfides inside the SEI, causing a minimal amount of polysulfides to travel across the electrolyte and to the lithium counter electrode. This in turns reduces the damage polysulfides can cause to the lithium SEI while also reducing temperature impact on the electrolyte. This is in good agreement with Fig. 24a and 24b, which show minimized capacity fluctuation in Method 3 batteries. Large difference exists between city and highway model CE because city model generates excess cycling stress compared to highway model. As shown in Fig. 24a-c and 24d, higher testing stress causes increased capacity and CE degradation rate.

4. Conclusion

We have demonstrated three different conditioning methods for Li-S batteries to study their effects on formation of the SEI layer for both anode and cathode. It was observed through the testing models, that plateau targeted conditioning (Method 3) creates a robust SEI layer on the sulfur and lithium electrode. We propose that this is attributed to the slower rate, targeting the second plateau, allocating more time for steady formation of the SEI layer while reducing time spent in the first plateau associated with long chain polysulfides. The resulting SEI layer suppresses the diffusion of polysulfides out of the cathode onto the lithium electrode, improves ionic pathways, maintains mechanical integrity, increases capacity, and enhances cycling stability of the Li-S battery. Additionally, this technique bypasses the use of additives and their associated adverse effects. In conclusion, plateau targeted conditioning provides the field of energy storage a novel, facile approach to improve battery performance.

References

1 Wild, M. *et al.* Lithium sulfur batteries, a mechanistic review. *Energy & Environmental Science* **8**, 3477-3494 (2015).

2 Zhang, S. S. Liquid electrolyte lithium/sulfur battery: fundamental chemistry, problems, and solutions. *Journal of Power Sources* **231**, 153-162 (2013).

3 Islam, M. M. *et al.* ReaxFF molecular dynamics simulations on lithiated sulfur cathode materials. *Physical Chemistry Chemical Physics* **17**, 3383-3393 (2015).

4 Cheon, S.-E. *et al.* Rechargeable lithium sulfur battery II. Rate capability and cycle characteristics. *Journal of The Electrochemical Society* **150**, A800-A805 (2003).

5 Yamin, H., Gorenshtein, A., Penciner, J., Sternberg, Y. & Peled, E. Lithium sulfur battery oxidation/reduction mechanisms of polysulfides in THF solutions. *Journal of the Electrochemical Society* **135**, 1045-1048 (1988).

6 Mikhaylik, Y. V. & Akridge, J. R. Polysulfide shuttle study in the Li/S battery system. *Journal of the Electrochemical Society* **151**, A1969-A1976 (2004).

7 Xiao, L. *et al.* A soft approach to encapsulate sulfur: polyaniline nanotubes for lithium-sulfur batteries with long cycle life. *Advanced Materials* **24**, 1176-1181 (2012).

8 Guo, J., Xu, Y. & Wang, C. Sulfur-impregnated disordered carbon nanotubes cathode for lithium–sulfur batteries. *Nano letters* **11**, 4288-4294 (2011).

9 Chen, S.-R. *et al.* Ordered mesoporous carbon/sulfur nanocomposite of high performances as cathode for lithium–sulfur battery. *Electrochimica Acta* **56**, 9549-9555 (2011).

10 Bauer, I., Thieme, S., Brückner, J., Althues, H. & Kaskel, S. Reduced polysulfide shuttle in lithium–sulfur batteries using Nafion-based separators. *Journal of Power Sources* **251**, 417-422 (2014).

11 Wang, H. *et al.* Graphene-wrapped sulfur particles as a rechargeable lithium–sulfur battery cathode material with high capacity and cycling stability. *Nano letters* **11**, 2644-2647 (2011).

12 Millner, A. in *Innovative Technologies for an Efficient and Reliable Electricity Supply (CITRES), 2010 IEEE Conference on.* 349-356 (IEEE).

13 Kong, W., Li, H., Huang, X. & Chen, L. Gas evolution behaviors for several cathode materials in lithium-ion batteries. *Journal of power sources* **142**, 285-291 (2005).

14 Li, W. *et al.* The synergetic effect of lithium polysulfide and lithium nitrate to prevent lithium dendrite growth. *Nature communications* **6** (2015).

15 Lin, Z., Liu, Z., Fu, W., Dudney, N. J. & Liang, C. Phosphorous pentasulfide as a novel additive for high-performance lithium-sulfur batteries. *Advanced Functional Materials* **23**, 1064-1069 (2013).

16 Wu, F. *et al.* Lithium iodide as a promising electrolyte additive for lithium–sulfur batteries: mechanisms of performance enhancement. *Advanced Materials* **27**, 101-108 (2015).

17 Scheers, J., Fantini, S. & Johansson, P. A review of electrolytes for lithium–sulphur batteries. *Journal of Power Sources* **255**, 204-218 (2014).

18 Ding, N. *et al.* Building better lithium-sulfur batteries: from LiNO3 to solid oxide catalyst. *Scientific reports* **6**, 33154 (2016).

19 Ji, L. *et al.* Porous carbon nanofiber–sulfur composite electrodes for lithium/sulfur cells. *Energy & Environmental Science* **4**, 5053-5059 (2011).

20 Xiang, H. *et al.* Enhanced charging capability of lithium metal batteries based on lithium bis (trifluoromethanesulfonyl) imide-lithium bis (oxalato) borate dual-salt electrolytes. *Journal of Power Sources* **318**, 170-177 (2016).

21 Pang, Q., Kundu, D. & Nazar, L. F. A graphene-like metallic cathode host for long-life and high-loading lithium–sulfur batteries. *Materials Horizons* **3**, 130-136 (2016).

22 Liang, X., Garsuch, A. & Nazar, L. F. Sulfur Cathodes Based on Conductive MXene Nanosheets for High-Performance Lithium–Sulfur Batteries. *Angewandte Chemie International Edition* **54**, 3907-3911 (2015).

23 Liang, X. *et al.* A highly efficient polysulfide mediator for lithium–sulfur batteries. *Nature communications* **6** (2015).

24 Pang, Q. *et al.* A Nitrogen and Sulfur Dual-Doped Carbon Derived from Polyrhodanine@ Cellulose for Advanced Lithium–Sulfur Batteries. *Advanced Materials* **27**, 6021-6028 (2015).

25 Tesla. *Tesla.com*, <https://www.tesla.com/models> (2017).

26 Chen, J.-J. *et al.* Conductive Lewis Base Matrix to Recover the Missing Link of Li2S8 during the Sulfur Redox Cycle in Li–S Battery. *Chemistry of Materials* **27**, 2048-2055 (2015).

27 Deng, Z. *et al.* Electrochemical impedance spectroscopy study of a lithium/sulfur battery: modeling and analysis of capacity fading. *Journal of The Electrochemical Society* **160**, A553-A558 (2013).

28 Yan, C. *et al.* Lithium metal protection through in-situ formed solid electrolyte interphase in lithium-sulfur batteries: The role of polysulfides on lithium anode. *Journal of Power Sources* **327**, 212-220 (2016).

29 Delpuech, N. *et al.* Mechanism of Silicon Electrode Aging upon Cycling in Full Lithium-Ion Batteries. *ChemSusChem* (2016).

30 Chang, D.-R., Lee, S.-H., Kim, S.-W. & Kim, H.-T. Binary electrolyte based on tetra (ethylene glycol) dimethyl ether and 1, 3-dioxolane for lithium–sulfur battery. *Journal of Power Sources* **112**, 452-460 (2002).

31 Markevich, E., Salitra, G., Talyosef, Y., Chesneau, F. & Aurbach, D. On the Mechanism of Quasi-Solid-State Lithiation of Sulfur Encapsulated in Microporous Carbons: Is the Existence of Small Sulfur Molecules Necessary? *Journal of The Electrochemical Society* **164**, A6244-A6253 (2017).

32 Liu, N. *et al.* A yolk-shell design for stabilized and scalable Li-ion battery alloy anodes. *Nano letters* **12**, 3315-3321 (2012).

33 Skoog, D. A., Holler, F. J. & Crouch, S. R. *Principles of instrumental analysis*. (Cengage learning, 2017).

34 Su, Y.-S. & Manthiram, A. A new approach to improve cycle performance of rechargeable lithium–sulfur batteries by inserting a free-standing MWCNT interlayer. *Chemical Communications* **48**, 8817-8819 (2012).

35 Dees, D. W., Kawauchi, S., Abraham, D. P. & Prakash, J. Analysis of the Galvanostatic Intermittent Titration Technique (GITT) as applied to a lithium-ion porous electrode. *Journal of Power Sources* **189**, 263-268 (2009).

36 Park, M.-S. *et al.* Porous carbon spheres as a functional conducting framework for use in lithium–sulfur batteries. *RSC Advances* **3**, 11774-11781 (2013).

37 Lee, S.-B. & Pyun, S.-I. The effect of electrolyte temperature on the passivity of solid electrolyte interphase formed on a graphite electrode. *Carbon* **40**, 2333-2339 (2002).

38 Li, N. *et al.* High-rate lithium–sulfur batteries promoted by reduced graphene oxide coating. *Chemical Communications* **48**, 4106-4108 (2012).

3.2.1 Supplementary Information

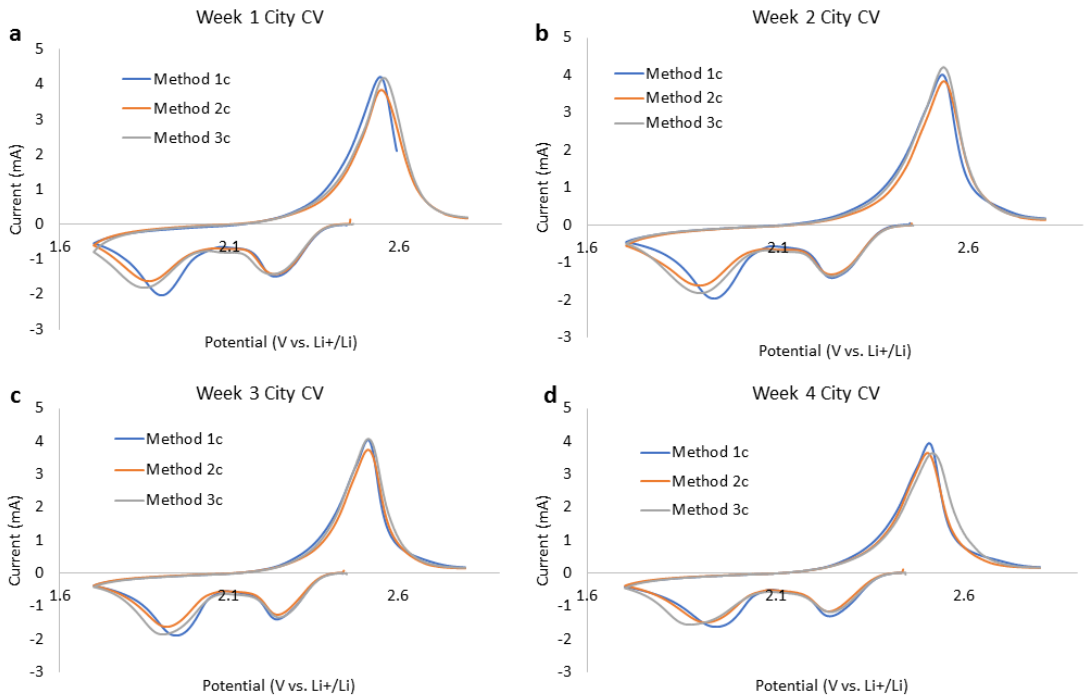

Figure 25: CV for Methods 1,2, & 3 batteries after (a) week 1, (b) week 2, (c) week 3 and (d) week 4 of city model driving.

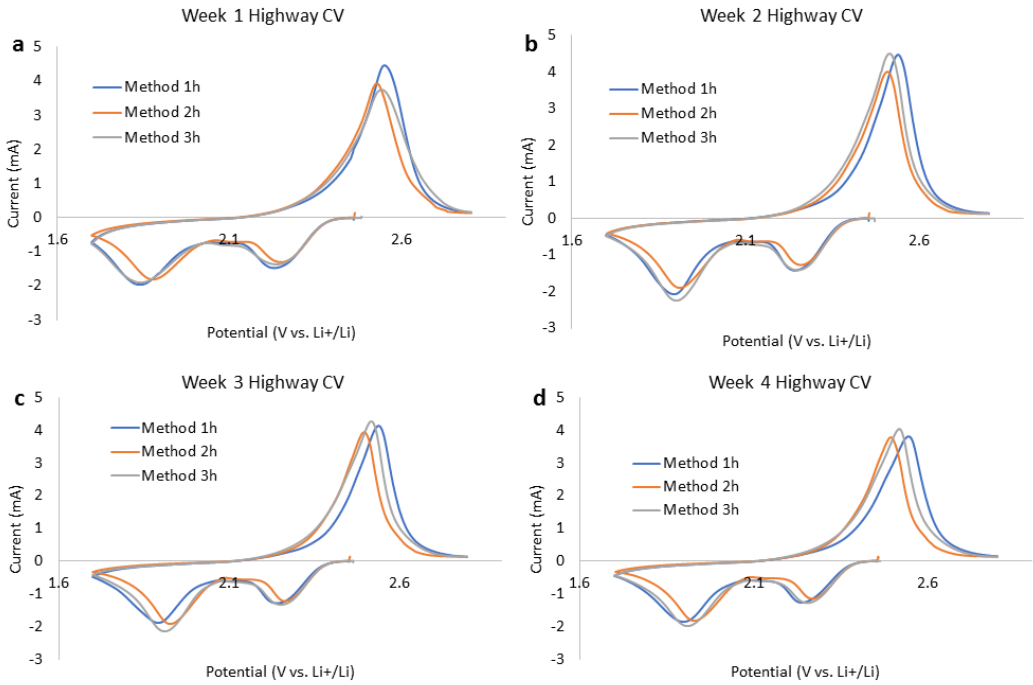

Figure 26: CV for Methods 1,2, & 3 batteries after (a) week 1, (b) week 2, (c) week 3 and (d) week 4 of highway model driving.

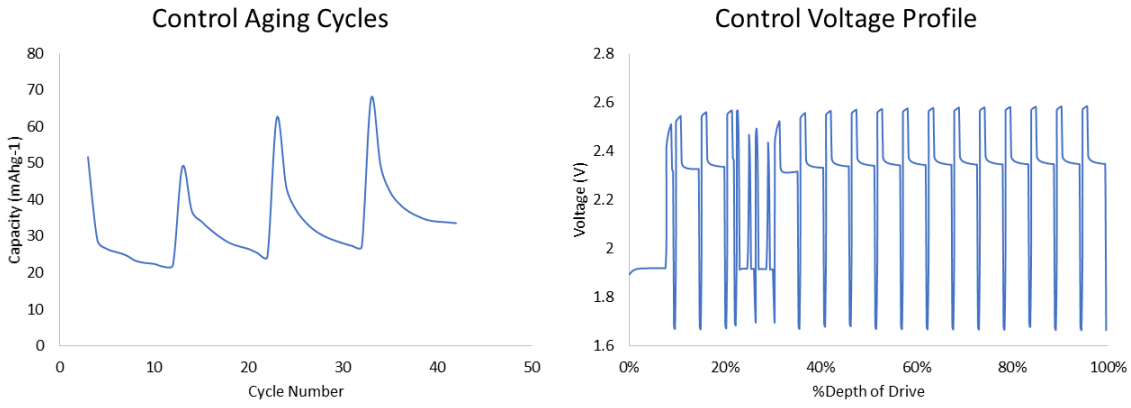

Figure 27: Aging cycle capacity and voltage profile during highway driving of control battery

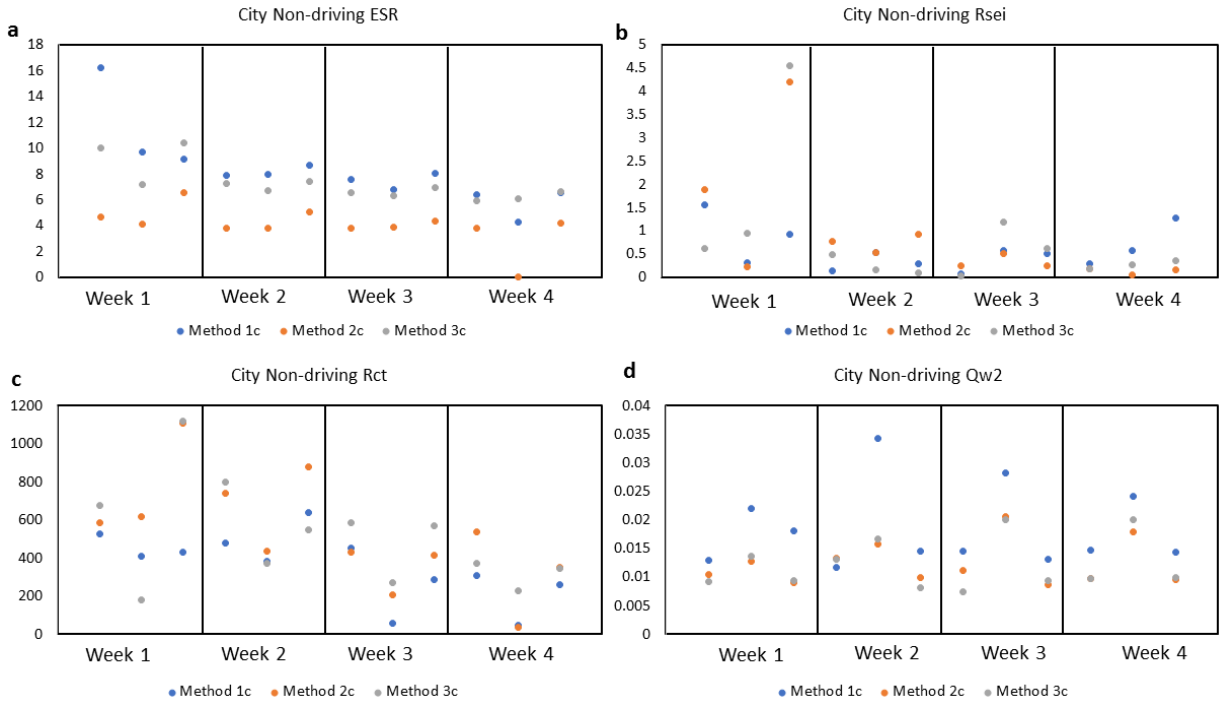

Figure 28: Impedance parameters of batteries tested by the city model after each GITT, aging cycle, and CV test (a) ESR. (b) Rsei. (c) Rct. (d) Qw2.

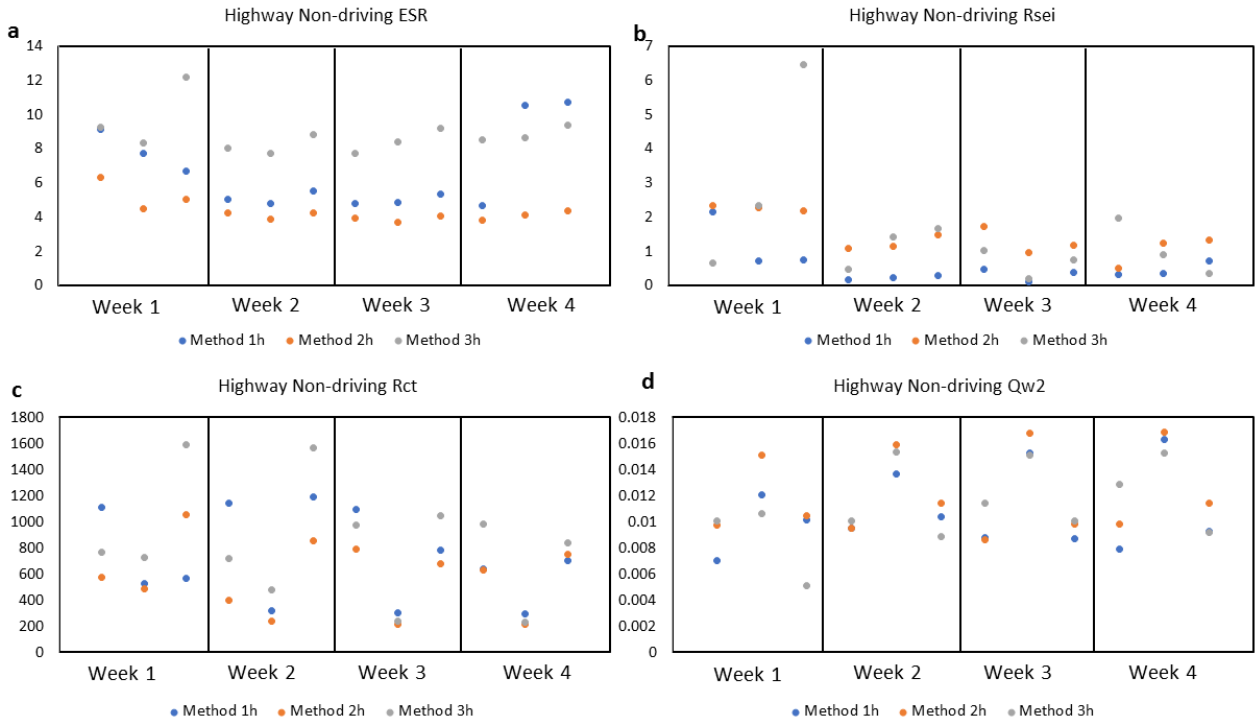

Figure 29: Impedance parameters of batteries tested by the highway model after each GITT, aging cycle, and CV test (a) ESR. (b) Rsei. (c) Rct. (d) Qw2.

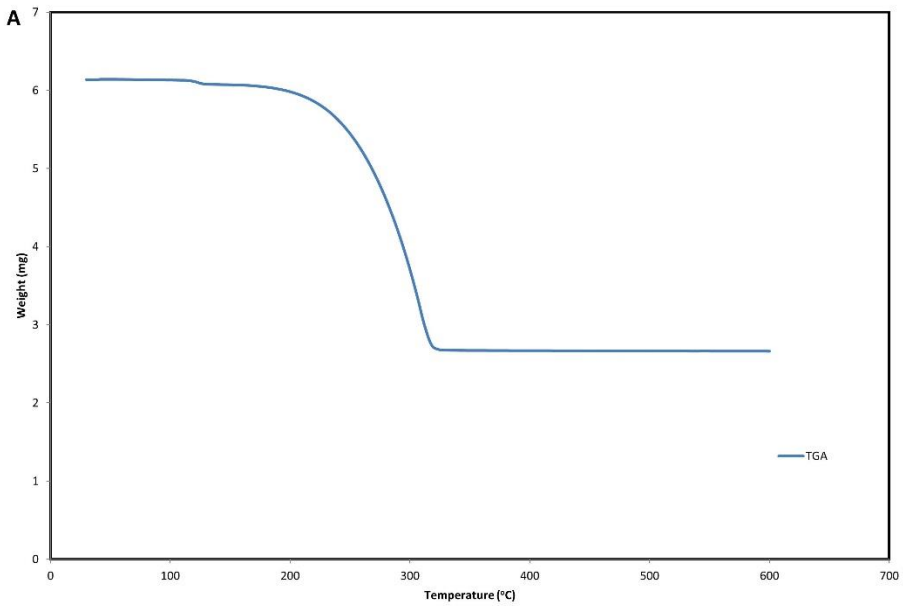

Figure 30: Thermogravimetric analysis of acetylene black sulfur composite

Table 3. Current rate used to simulate corresponding driving speed

Current Model		
MPH	**Distance(mi)**	**C-Rate**
5	1440.4	C/288.1
10	1142.4	C/114.2
15	968.0	C/64.5
20	844.3	C/42.2
25	748.4	C/29.9
30	670.0	C/22.3
35	603.7	C/17.2
40	546.3	C/13.7
45	496.0	C/11.0
50	451.0	C/9.0

55	409.0	C/7.4
60	371.0	C/6.2
65	337.0	C/5.2
70	307.0	C/4.4
75	276.0	C/3.7
80	248.2	C/3.1

4. The Future of Batteries, a short Perspective

Current research on next generation battery materials, such as silicon and sulfur, show promise towards higher energy densities batteries but are still a long ways out. At the current rate of development, silicon will be continually introduced into the anode at higher weight percentages providing increased performance with the expectation of 100% weight silicon anodes in 4-5 years. Sulfur cathodes on the other hand aren't expected to research the level of stability needed for commercialization in an aggressive consumer market for at least another 10 years. Lithium metal will have special circumstances surrounding its adoption. As it stands, lithium metal has to many problems to solve with one "cure all" method. The use of costly additives or exotic host structures is contrary to easily manufactured materials. Ergo, lithium metal in recent years will most likely only see use in one off batteries with a short duty cycle mostly likely for applications in Military or Defense. The "Holy Grail" of an environmentally benign Sulfur-Silicon Full Cell is at least 15 years off. Current research into the structure is still at the early theoretical stages with very little fundamental research taking place on the subject matter. Most researcher view it too complicated of a system and feel sulfur will naturally be paired with lithium due to the benefits of polysulfides on lithium dendrite formation.

A brief Summation of the order of development and adoption is Silicon, lithium, Non-natively oxidized silicon, Sulfur, then Sulfur-Silicon. Although this is a very broad

statement and there will be changes in electrolyte, binder, and separator, the main material systems will most likely follow this order as it is the logical progression in terms of incremental increases in energy density.